Impacts of basal melting of the Totten Ice Shelf and biological productivity on marine biogeochemical components in Sabrina Coast, East Antarctica

Tetsuya P Tamura[1,1], Daiki Nomura[1,1], Daisuke Hirano[2,2], Takeshi Tamura[2,2], Masaaki Kiuchi[1,1], Gen Hashida[3,3], Ryosuke Makabe[4,4], Kazuya Ono[1,1], Shuki Ushio[2,2], Kaihe Yamazaki[1,1], Yoshihiro Nakayama[5,5], Keigo D Takahashi[2,2], Hiroko Sasaki[6,6], Hiroto Murase[7,7], and Shigeru Aoki[1,1]

[1]Hokkaido University
[2]National Institute of Polar Research
[3]National Institute for Polar Research
[4]National Institute of Polar Research, Japan
[5]Institute of Low Temperature Science
[6]Japan Fisheries Research and Education Agency
[7]Tokyo University of Marine Science and Technology

January 20, 2023

Abstract

To clarify the impact of basal melting of the Antarctic ice sheet and biological productivity on biogeochemical processes in Antarctic coastal waters, concentrations of dissolved inorganic carbon (DIC), total alkalinity (TA), inorganic nutrients, chlorophyll *a*, and stable oxygen isotopic ratios ($\delta^{18}O$) were measured from the offshore slope to the ice front of the Totten Ice Shelf (TIS) during the spring/summer of 2018, 2019, and 2020. Off the TIS, modified Circumpolar Deep Water (mCDW) intruded onto the continental shelf and flowed along bathymetric troughs into the TIS cavity, where it met the ice shelf base and formed a buoyant mixture with glacial meltwater. Physical oceanographic processes mostly determined the distributions of DIC, TA, and nutrient concentrations. However, DIC, TA, and nutrient concentrations on the surface of the ice front were decreased by photosynthesis and the dilution effect of meltwater from sea ice and the base of the ice shelf. The partial pressure of CO_2 (pCO_2) in surface water was reduced by photosynthesis and dilution, and the surface water became a strong CO_2 sink for the atmosphere. The DIC and TA (normalized to salinity of 34.3 to correct for dilution effects) changed in a molar ratio of 106:16 because of phytoplankton photosynthesis. The decrease of pCO_2 by more than 100 µatm with respect to mCDW was thus the result of photosynthesis. The nutrient consumption ratio suggested that enough iron was present in the water column to supply the surface layer via buoyancy-driven upwelling and basal melting of the TIS.

Hosted file

`table1.docx` available at https://authorea.com/users/534203/articles/598413-impacts-of-basal-melting-of-the-totten-ice-shelf-and-biological-productivity-on-marine-biogeochemical-components-in-sabrina-coast-east-antarctica

Hosted file

`support infomation tamura p et al.docx` available at https://authorea.com/users/534203/articles/598413-impacts-of-basal-melting-of-the-totten-ice-shelf-and-biological-

productivity-on-marine-biogeochemical-components-in-sabrina-coast-east-antarctica

Impacts of basal melting of the Totten Ice Shelf and biological productivity on marine biogeochemical components in Sabrina Coast, East Antarctica

Tetsuya P. Tamura[1], Daiki Nomura[2, 1, 3], Daisuke Hirano[4, 5], Takeshi Tamura[4, 5], Masaaki Kiuchi[1], Gen Hashida[4], Ryosuke Makabe[4, 5, 6], Kazuya Ono[7], Shuki Ushio[4], Kaihe Yamazaki[7], Yoshihiro Nakayama[7], Keigo D. Takahashi[5], Hiroko Sasaki[8], Hiroto Murase[6], and Shigeru Aoki[7]

[1]Faculty of Fisheries Science, Hokkaido University, Hakodate, Japan, [2]Field Science Center for Northern Biosphere, Hokkaido University, Hakodate, Japan, [3]Arctic Research Center, Hokkaido University, Sapporo, Japan, [4]National Institute of Polar Research, Tachikawa, Japan, [5]Graduate University for Advanced Studies (SOKENDAI), Tachikawa, Japan, [6]Tokyo University of Marine Science and Technology, Tokyo, Japan, [7]Institute of Low Temperature Science, Hokkaido University, Sapporo, Japan, [8]Fisheries Resources Institute, Japan Fisheries Research and Education Agency, Yokohama, Japan.

Correspondence to: D. Nomura, daiki.nomura@fish.hokudai.ac.jp

Abstract To clarify the impact of basal melting of the Antarctic ice sheet and biological productivity on biogeochemical processes in Antarctic coastal waters, concentrations of dissolved inorganic carbon (DIC), total alkalinity (TA), inorganic nutrients, chlorophyll *a*, and stable oxygen isotopic ratios ($\delta^{18}O$) were measured from the offshore slope to the ice front of the Totten Ice Shelf (TIS) during the spring/summer of 2018, 2019, and 2020. Off the TIS, modified Circumpolar Deep Water (mCDW) intruded onto the continental shelf and flowed along bathymetric troughs into the TIS cavity, where it met the ice shelf base and formed a buoyant mixture with glacial meltwater. Physical oceanographic processes mostly determined the distributions of DIC, TA, and nutrient concentrations. However, DIC, TA, and nutrient concentrations on the surface of the ice front were decreased by photosynthesis and the dilution effect of meltwater from sea ice and the base of the ice shelf. The partial pressure of CO_2 (pCO_2) in surface water was reduced by photosynthesis and dilution, and the surface water became a strong CO_2 sink for the atmosphere. The DIC and TA (normalized to salinity of 34.3 to correct for dilution effects) changed in a molar ratio of 106:16 because of phytoplankton photosynthesis. The decrease of pCO_2 by more than 100 μatm with respect to mCDW was thus the result of photosynthesis. The nutrient consumption ratio suggested that enough iron was present in the water column to supply the surface layer via buoyancy-driven upwelling and basal melting of the TIS.

Plain abstract:

Oceanographic observations were made from the offshore continental slope to the Totten Ice Shelf (TIS) front in Sabrina Coast, East Antarctica, during spring/summer 2018, 2019 and 2020. Results revealed that surface water was strongly influenced by phytoplankton activity and the dilution effect of meltwater from sea ice and the base of the ice shelf. The nutrient consumption ratio between the winter water near the TIS front and surface water suggested that enough iron was present in the water column to stimulate photosynthesis. The iron was introduced into the surface layer by buoyancy-driven upwelling and the basal melting of the TIS.

Keywords: Totten Ice Shelf, basal melting, biogeochemical components, biological productivity, Southern Ocean

Key points:

- The inflow of modified Circumpolar Deep Water supplied biogeochemical components under the Totten Ice Shelf.
- Surface water was influenced by dilution from ice shelf basal meltwater and sea ice meltwater and was changed by biological productivity.
- Buoyancy-driven upwelling and basal melting of the Totten Ice Shelf introduced sufficient iron to surface water to stimulate photosynthesis.

1. Introduction

Compared to the open ocean area of the Southern Ocean, which is responsible for half of the atmospheric CO_2 absorption by the entire ocean, the air–sea CO_2 flux in the coastal region significantly changes on a seasonal basis. As an annual average, it is a small carbon sink (Takahashi et al., 2012). The biogeochemical components of the carbon cycle in the open-water areas have been quantitatively evaluated. However, in the seasonal ice areas and areas covered with year-round sea ice, in-situ data are insufficient to fully describe the ocean carbon cycle (Lenton et al., 2013). In particular, the rapid melting of ice shelves in recent years (e.g., Pritchard et al., 2012; Rignot et al., 2019) has provided huge amounts of freshwater to the coastal areas of the Southern Ocean, and there are concerns about the effects of that freshwater on the marine environment and biogeochemical components.

There are many coastal polynyas around Antarctica (Tamura et al., 2008). In polynyas, primary production by phytoplankton has been shown to be related to the melting rates of adjacent ice shelves and sea ice (Arrigo et al., 2015; Moreau et al., 2019). Primary production in most of the Southern Ocean is low because of iron limitation, and high production is limited to areas where iron is supplied to the surface layer (de Baar et al., 1990). Sources of iron to the surface water are basal melting of ice shelves and subglacial discharged water (Arrigo et al., 2015; Herraiz-Borreguero et al., 2016), atmospheric dust (Jickells et al., 2005), vertical mixing in winter (Tagliabue et al., 2014), upwelling associated with fronts (Schallenberg et al. 2018), and melting of sea ice (Duprat et al., 2020; Lannuzel et al., 2007). Basal melting of ice shelves is considered to be the main source of iron near the Antarctic coast (Arrigo et al., 2015). In the Pine Island Polynya and Amundsen Polynya in West Antarctica, where the primary productivity is highest in the Antarctic coast, sediment-derived iron is supplied by mixing with the ice shelf basal meltwater in the adjacent ice shelf. When iron is supplied, primary production is high (Gerringa et al., 2012; Oliver et al., 2019; St-Laurent et al., 2019). Ice-core drilling at Amery Ice Shelf in East Antarctica has revealed the iron-rich marine ice at the ice shelf base, created by subglacial discharged

water. Its melting supplies iron to the ocean surface, resulting in the high primary production around the Amery Ice Shelf (Herraiz-Borreguero et al., 2016).

Our research group has investigated the reduction of the partial pressure of CO_2 (pCO_2) due to the effect of dilution by glacier meltwater near the Shirase Glacier Tongue in Lützow-Holm Bay, East Antarctica (Kiuchi et al., 2021). In this area, the inflow of modified Circumpolar Deep Water (mCDW) from the outer edge of the continental shelf to the bottom of the ice shelf is a major cause of significant melting at the bottom of the ice shelf (Hirano et al., 2020). mCDW is mixed with the meltwater from the ice shelf and becomes fresher and lighter, then upwells along the ice shelf base. This vertical circulation is called the ice pump (Lewis and Perkin, 1986). In this process, the dissolved inorganic carbon (DIC) and total alkalinity (TA) of the seawater are diluted by the glacial meltwater supply. As a result, a pCO_2 that was originally 431 ± 12 μatm in mCDW decreases by 42 ± 2 μatm because of the influence of the meltwater (Kiuchi et al., 2021). It is therefore clear that variations of the supply of glacial meltwater cause wide fluctuations in the carbonate chemistry in the area where ice shelves have developed in the coastal seas of Antarctica, and those fluctuations affect the CO_2 exchange process between the atmosphere and the ocean.

The Totten Ice Shelf (TIS), focused in this study, is the terminus of the Totten Glacier in East Antarctica. If the entire ice sheet behind the TIS were to flow into the ocean, the global rise of sea level would be ~3.5 m (Li et al., 2015; Greenbaum et al., 2015). Basal melting of the TIS occurs by the warm mCDW flows onto the continental shelf (Hirano et al., 2021) and intrudes the ice cavity (Rintoul et al., 2016; Silvano et al., 2017). Various studies have recently been conducted on the mCDW pathways, and it has been shown that mCDW is transported across the continental slope and intrudes the coastal area (Nitsche et al., 2017; Silvano et al., 2019). Measurements of biogeochemical components near the TIS were previously made by the icebreaker *Aurora Australis* in January 2015. According to Aroyo et al. (2019), who reported the carbonate chemistry near the TIS, the surface of the ice front was covered by sea ice even in the summer, and primary production by phytoplankton was limited by the low-light conditions. Therefore, the surface water pCO_2 was supersaturated with respect to the atmosphere.

However, knowledge of the cross-shelf characteristics of the carbonate chemistry and biogeochemical components is lacking. It allows evaluating the effect of dilution by the ice shelf basal meltwater on the carbonate chemistry and the primary production by phytoplankton. In addition, the components of the carbonate chemistry have been measured only once on the TIS front (Aroyo et al., 2019), and seasonal changes due to the presence or absence of sea ice have not been documented.

In this study, we sampled the offshore water intruding the TIS cavity and evaluated the impact of the alteration of the process of inflow to the ice front and of the melting of the TIS, which has a high basal melting rate, on the biogeochemical components of the surrounding sea. The observations were carried out from the shelf break of the Sabrina Coast to the TIS front. In addition, observations were conducted in December (early summer) and March (late summer) to investigate seasonal changes at the ice front. The effects of differences in the environment, such as the extent of sea ice on the carbonate chemistry, were investigated in detail by conducting the studies for multiple years. We also considered the role of iron supplied by glacier meltwater by examining the ratios of nutrients taken up by phytoplankton.

2. Materials and Methods

2.1. Sampling

Oceanographic observations were conducted on the continental shelf slope near the TIS in mid-February 2019 during the 10th Antarctic survey by R/V *Kaiyo Maru* of the Fisheries Agency (KY1804). Additional studies were carried out from the Japan Maritime Self-Defense Force icebreaker *Shirase* from the offshore slope to the front of the TIS in early March 2018 during the 59th Japanese Antarctic Research Expedition (JARE59) as well as in December 2019 and early March 2020 during the 61st Japanese Antarctic Research Expedition (JARE61) (Figure 1).

Vertical profiles of temperature and salinity were measured with a conductivity–temperature–depth (CTD) probe (SBE 9plus, Sea-Bird Electronics, Bellevue, WA, USA from the *Kaiyo-maru* and SBE19, Sea-Bird Electronics, Bellevue, WA, USA from the *Shirase*). In addition, seawater samples were taken to calibrate the salinity sensor. Seawater samples were collected vertically in rosette–mounted 10-L Niskin bottles (Ocean Test Equipment, Inc., Lauderdale, FL, USA) from the *Kaiyo-maru* and 4-L Niskin bottles (SBE55 ECO, Sea-Bird Electronics, Bellevue, WA, USA) from the *shirase*.

Seawater was subsampled into (1) a 200-mL glass vial (Maruemu Co., Ltd., Osaka, Japan) for measurement of dissolved inorganic carbon (DIC) and total alkalinity (TA), (2) a 15-mL glass screw-cap vial (Nichiden-Rika Glass Co. Ltd, Kobe, Japan) for measurement of the oxygen isotopic ratio ($\delta^{18}O$) of the water, (3) a 10-mL polyethylene screw-cap vial (Eiken Chemical Co. Ltd, Tokyo, Japan) for measurement of inorganic nutrients (NO_3^-, PO_4^{3-}, and $Si(OH)_4$), and (4) a 300-mL Nalgene polycarbonate bottle (Thermo Fisher Scientific Inc., Waltham, MA, USA) for measurement of chlorophyll *a* (chl.a) concentrations. Immediately after subsampling for measurement of DIC and TA, a 6.0% (wt.) mercury chloride ($HgCl_2$) solution (200 μL) was added to stop biological activity. Samples for DIC, TA, and $\delta^{18}O$ were stored at room temperature (+20°C). Samples for nutrient concentrations were stored in a freezer (–30°C). Samples for chl.a measurements were immediately filtered onto 25-mm diameter Whatman GF/F filters. The chlorophyll on the filters was then extracted with *N,N*–dimethylformamide (Suzuki and Ishimaru, 1990) for 24 h in a –80°C freezer.

2.2. Sample analysis

The concentrations of DIC were determined by coulometry (Johnson et al., 1985, 1992) using a hand-made CO_2 extraction system (Ono et al., 1998) and a coulometer (CM5012, UIC, Inc., Binghamton, NY, USA). The TA of the seawater was determined by titration (Dickson et al., 2007) with a TA analyzer (ATT-05, Kimoto Electric Co.,

Ltd., Japan). Both DIC and TA measurements were calibrated against reference seawater materials (Batch AO and AP; KANSO Technos Co., Ltd., Osaka, Japan) traceable to the certified reference material distributed by Prof. A. G. Dickson (Scripps Institution of Oceanography, La Jolla, CA, USA). The standard deviations of the DIC and TA measurements, calculated from the results for 10 subsamples of the reference water with DIC = 1987.1 μmol kg^{-1} and TA = 2257.6 μmol kg^{-1}, were less than 2.0 μmol kg^{-1} for both DIC and TA. The seawater pCO_2 was computed from DIC and TA using the program CO2SYS, version 02.05 (Orr et al., 2018). For this calculation, we used the carbonic acid dissociation constants (K_1 and K_2) of Mehrbach et al. (1973) as revised by Dickson and Millero (1987) and the K_{HSO4} value determined by Dickson (1990).

The seawater $\delta^{18}O$ was determined with a mass spectrometer (Isoprime precisION, Elementar, Stockport, UK) with the equilibration bath of 30.0°C. The $\delta^{18}O$ in permil (‰) was calculated using the ^{18}O:^{16}O ratio of Vienna standard mean ocean water (VSMOW2) as the standard. The average of at least three runs was adopted. The standard deviation of the averaged $\delta^{18}O$, calculated from 104 pairs of reference water with a $\delta^{18}O$ of +0.033‰, was 0.01‰.

The concentrations of NO_3^-, PO_4^{3-}, and $Si(OH)_4$ in the seawater were determined in accord with the Joint Global Ocean Flux Study (JGOFS) spectrophotometric method (JGOFS, 1994) using auto-analyzer systems: a QuAAtro 2-HR system (BL-tec, Osaka, Japan) and a Seal Analytical system (Norderstadt, Germany). The analyzers were calibrated with reference materials for nutrient analysis (Lots AW and BG; KANSO Technos Co., Ltd.). The standard deviations of the nutrient concentrations, calculated from 20 subsamples taken from reference water samples (KANSO Technos Co., Ltd.) with NO_3^-, PO_4^{3-}, and $Si(OH)_4$ concentrations of 9.8, 2.1, and 117.5 μmol L^{-1}, were 0.3, 0.1, and 1.1 μmol L^{-1}, respectively.

The concentrations of chl.a were determined with a fluorometer (Model 10AU, Turner Designs, Inc., Sunnyvale, CA, USA) by the method of Parsons et al. (1984). Standards (0.05–159 μg L^{-1} chl.a) prepared from a liquid chl.a standard (Wako Pure Chemical

Industries, Ltd., Osaka, Japan) by stepwise dilution with *N,N*-dimethylformamide were used to calibrate the fluorometer before chl.a measurements.

3. Results

3.1. Hydrographic and biogeochemical properties

3.1.1. Continental slope

On the continental shelf slope (corresponding to St. 501 to St. 529), the temperature and salinity of the surface layer (100–300 dbar) were low (Winter Water: WW), but in the subsurface layer (300–500 dbar) high (>1°C and >34.7, respectively), corresponding to mCDW (Figures 2a, b). In addition, at Stations 502, 507, 512, and 522, water masses with particularly high temperature (+1.2 to +1.4°C) were distributed in a core shape at 350–400 dbar (Figures 2a, b). The DIC and TA of the mCDW present in the subsurface layer (300–500 dbar) on the continental slope were 2251 ± 10 μmol kg^{-1} and 2363 ± 10 μmol kg^{-1}, respectively (mean ± standard deviation) (Figures 2c, d). The distributions of nutrient concentrations were similar to the distributions of DIC and TA; the concentrations were high in the mCDW (NO_3^-: 31.7 ± 1.1 μmol L^{-1}, PO_4^{3-}: 2.1 ± 0.1 μmol L^{-1}, Si $(OH)_4$: 93.6 ± 3.3 μmol L^{-1}) (Figures 2e–g).

3.1.2. TIS front and coastal area

In the TIS front and coastal areas, low-temperature and low-salinity WW was present in the surface layer (100–500 dbar) as well as on the continental slope (Figures 3, 4, 5, 6a, b). The presence of high-temperature and high-salinity mCDW in the bottom layer (~800 dbar) of the TIS front was consistent with the report of Rintoul et al. (2016). This mCDW had a lower temperature (<+0.16°C) and a lower salinity (<34.62) than the mCDW (Figures 2a, b) on the outer edge of the continental shelf (Figures 3, 4a, b).

The DIC concentration on the TIS front and in coastal surface water (20 dbar) was 2086 ± 12 μmol kg^{-1} (Figures 3, 4, 6c) in March. In March 2018, the DIC concentration tended to decrease at the stations furthest to the west: St. TT2 (2079 μmol kg^{-1}) and St. TT3 (2068 μmol kg^{-1}) (Figure 3c). The DIC was 2202 ± 4 μmol kg^{-1} in the WW at 200 dbar and 2233 ± 6 μmol kg^{-1} in the mCDW present in the bottom trough. The TA followed a pattern similar to that of the DIC, low on the surface (2253 ± 11 μmol kg^{-1}) and high in mCDW (2337 ± 7 μmol kg^{-1}) (Figures 3, 4, 6d). The distribution of nutrient concentrations was similar to the distributions of DIC and TA. The concentrations were low at the surface (NO_3^-: 20.5 ± 1.9 μmol L^{-1}, PO_4^{3-}: 1.38 ± 0.10 μmol L^{-1}, $Si(OH)_4$: 45.0 ± 0.7 μmol L^{-1}) (Figures 3, 4, 6h–j). The concentrations were higher in mCDW (NO_3^-: 33.6 ± 0.7 μmol L^{-1}, PO_4^{3-}: 2.21 ± 0.08 μmol L^{-1}, $Si(OH)_4$: 89.5 ± 8.0 μmol L^{-1}) (Figure 6h–j). The $\delta^{18}O$ was high in the surface layer and was vertically uniform in WW. The $\delta^{18}O$ was higher in the deep mCDW than in both surface mCDW and WW (Figure 6g). The vertical profiles of chl.*a* concentrations at 0–100 dbar showed different distribution and concentration among years (Figure 6k). On average, the chl.*a* concentrations for each depth in 2018 was about twice those of the other two years. The averaged profiles showed that chl.*a* decreased at greater depth and reached the minimum at 100 dbar, although some profiles in 2018 had chl.*a* maxima at 50 dbar.

Figure 6 also shows vertical profiles of the various characteristics of the water for December and March on the ice front and in coastal areas. On the ice front, the water temperature increased from –1.5°C to –1.1°C in the surface layer (0–100 dbar) from December to March, and the salinity decreased from 34.0 to 33.0 (Figures 5, 6a, b). The salinity reduction was likely due to the rise in water temperature from December to March and the accompanying increase in meltwater input. In contrast, at depths below 100 dbar, the water temperature and salinity were almost constant (–1.78 ± 0.06°C, 34.23 ± 0.04). From December to March, surface DIC, TA, and nutrient concentrations decreased (Figures 6c, d, h–j), but below 100 dbar, they remained constant, as did temperature and salinity. The $\delta^{18}O$ also decreased in the surface layer (Figure 6g).

From December to March, the salinity of the surface layer decreased due to the increase

in meltwater accompanying the rise in water temperature. Therefore, to remove the dilution effect of DIC and TA by mixing glacier and sea ice with meltwater from winter to summer, we normalized the DIC and TA to a salinity of 34.3 (34.3 was used in Arroyo et al. (2019); Figures 6e, f). At depths below 100 dbar, there was no change in nDIC and nTA, but on the surface, nDIC decreased and nTA increased from December to March. Table 1 lists the mean and standard deviations for DIC, TA, $\delta^{18}O$, NO_3^-, PO_4^{3-}, and $Si(OH)_4$ for each water mass and month.

3.1.3. From the continental slope to the ice front and coastal areas

Figure 7 shows various cross-sectional views from the continental slope to the ice front and coastal areas. Low-temperature, low-salinity WW was present up to about 500 dbar (Figures 7a, b). The high-temperature, high-salinity mCDW near the seafloor below 500 dbar on the ice front was continuously extended from offshore mCDW at the continental slope. The property of mCDW became colder (<+0.16°C) and fresher (<34.62) from the continental slope to the ice front and coastal areas (Figures 7a, b). The distributions of the biogeochemical properties and hydrographic properties were very similar (Figures 7c–g). The concentrations of biogeochemical properties in the mCDW on the continental shelf and at the bottom of the ice front were high. However, the concentrations of biogeochemical properties of the mCDW were lower at the bottom of the ice front on the continental shelf. In contrast, there were places where the concentrations of NO_3^- and PO_4^{3-} in the mCDW were higher at the bottom of the ice front than on the continental shelf (Figures 7c, f).

4. Discussion

4.1. Variation of pCO_2 by the dilution effect

The dilution effect of ice shelf meltwater and sea ice meltwater is known as one of the

important processes affecting the carbonate chemistry in the ocean surface layer along the Antarctic coast in summer (e.g., Legge et al., 2017; Shadwick et al., 2017; Arroyo et al., 2019; Kiuchi et al., 2021). In this study, observations in December and March showed a decrease of DIC and TA with decreasing salinity. Because these changes could be caused by sea ice meltwater or TIS basal meltwater, we quantitatively evaluate the fraction of TIS basal meltwater, sea ice meltwater, and mCDW in the collected water samples by using salinity and $\delta^{18}O$ (e.g., Meredith et al., 2008) and the following equations.

$$F_{mCDW} + F_{gmw} + F_{siw} = 1 \quad (1)$$

$$F_{mCDW} \cdot S_{mCDW} + F_{gmw} \cdot S_{gmw} + F_{simw} \cdot S_{simw} = S_{obs} \quad (2)$$

$$F_{mCDW} \cdot \delta_{mCDW} + F_{gmw} \cdot \delta_{gmw} + F_{simw} \cdot \delta_{simw} = \delta_{obs} \quad (3)$$

where F_{mCDW}, F_{gmw}, and F_{siw} are fractions of mCDW, TIS basal meltwater as glacier meltwater, and sea ice meltwater, respectively. The S_{mCDW}, S_{gmw}, and S_{simw} are the salinities of each end-member, and δ_{mCDW}, δ_{gmw}, and δ_{simw} are the $\delta^{18}O$ values of each end-member. S_{obs} and δ_{obs} are the observed salinity and $\delta^{18}O$, respectively, of the samples. The end-member values in this study were set as follows: mCDW (S_{mCDW} = 34.69, δ_{mCDW} = –0.06‰) (mean value of St. 522 at 350–400 dbar), gmw (S_{gmw} = 0.0 , δ_{gmw} = –30‰) (Silvano et al., 2018), and simw (S_{simw} = 1.2, δ_{simw} = +6.2‰) (Silvano et al., 2018). Kiuchi et al. (2021) have pointed out that the δ_{gmw} is the most uncertain end-member and could lie anywhere between −40‰ and −20‰ (Silvano et al., 2018). In our study, we chose an intermediate value of −30‰ for δ_{gmw}. To evaluate the effect of using other end-members within this range, we also calculated fractions based on δ_{gmw} ranging between −40‰ and −20‰. This analysis suggested that our choice of δ_{gmw} = −30‰ is accurate to 1.1% fraction. We also calculated the fraction changes due to the $\delta^{18}O$ variation within its standard deviation and the choice of mCDW end-member (i.e., δ_{mCDW} = –0.06 ± 0.005‰). The estimated potential errors were less than 0.1% for the

$\delta^{18}O$ measurement and 0.3% for the end-member of mCDW.

Figures 8a–c show F_{gmw}, F_{simw}, and F_{mCDW} in the TIS front and coastal areas. The F_{gmw} in the surface layer (20 dbar) in March 2018 was 1.53 ± 0.09% (mean ± standard deviation for all stations). The F_{gmw} in March 2020 was 1.64 ± 0.03%, which was similar value in March 2018. The F_{gmw} in December 2019 was 1.67 ± 0.09%. Therefore, there was no seasonal change between December and March. The F_{gmw} was slightly lower in the middle layer (200–500 dbar) than in the surface layer and was uniformly distributed vertically. In addition, the F_{gmw} was +0.32% or more, even in the deep layer. The implication is that the mCDW that flowed in from the outer edge of the continental shelf was diluted under the influence of meltwater in the process of flowing under the TIS. The F_{simw} in the surface layer (20 dbar) in March 2018 was 2.91 ± 0.13%, and the F_{simw} in March 2020 was 3.87 ± 0.05%. Therefore, sea ice melting was more active in 2020 than in 2018. However, the F_{simw} in December 2019 was as low as 0.18 ± 0.20%.

Figures 8d–i show the longitudinal distributions of F_{gmw} and F_{simw}. F_{gmw} in the surface layer (20 dbar) in March 2018 was low (1.44–1.47%) on the east side of the study area (Sts. TT1, 4, 5, and 6) and high (1.63–1.67%) on the west side (Sts. TT2 and 3) (Figure 8d). This pattern suggests that a large amount of meltwater generated by basal melting by the mCDW flowed from the east side to the west side of the TIS.

Next, we quantitatively evaluated the effects of TIS basal meltwater and sea ice meltwater on the carbonate chemistry from the relationship between F_{gmw}, F_{siw}, DIC/TA, and salinity.

$$\Delta S_{gmw} = -F_{gmw} \cdot 10^{-2} \cdot S_{mCDW} \quad (4)$$

$$\Delta S_{simw} = -F_{simw} \cdot 10^{-2} \cdot S_{mCDW} + F_{simw} \cdot 10^{-2} \cdot S_{simw} \quad (5)$$

$$\Delta DIC_{mix} = \Delta S_{gmw} \text{ or } \Delta S_{simw} \cdot M_{DIC-S} \quad (6)$$

$$\Delta TA_{mix} = \Delta S_{gmw} \text{ or } S_{simw} \cdot M_{TA-S} \quad (7)$$

In the above equations, ΔS_{gmw} and ΔS_{simw} are changes of salinity by glacier meltwater and sea ice meltwater, respectively. ΔDIC_{mix} and ΔTA_{mix} are changes of DIC and TA by mixing of glacier meltwater and sea ice meltwater with mCDW. M_{DIC-S} and M_{TA-S} are the slopes of the DIC–salinity and TA–salinity relationship between mCDW and origin.

Using the changes of ΔS_{gmw}, ΔS_{simw}, ΔDIC_{mix}, and ΔTA_{mix} calculated from Equations 4–7, we used CO2SYS, version 02.05 (Orr et al., 2018) to calculate the $pCO_{2\ gmw}$ when the mCDW flowing under the ice shelf was mixed with the basal meltwater of the TIS as well as the $pCO_{2\ simw}$ when the mCDW was mixed with sea ice meltwater.

$$\Delta pCO_{2\ gmw} = pCO_{2\ gmw} - pCO_{2\ mCDW} \quad (8)$$

$$\Delta pCO_{2\ simw} = pCO_{2\ simw} - pCO_{2\ mCDW} \quad (9)$$

$$\Delta pCO_{2\ gmw+\ simw} = \Delta pCO_{2\ gmw} + \Delta pCO_{2\ simw} \quad (10)$$

In Equations 8–10, $pCO_{2\ gmw}$ is the pCO_2 when mCDW is mixed with ice shelf basal meltwater, $pCO_{2\ simw}$ is the pCO_2 when mCDW is mixed with sea ice meltwater, and $pCO_{2\ mCDW}$ is an observation point on the offshore slope (St. 522) (451 ± 14 µatm at 350–400 dbar). $\Delta pCO_{2\ gmw}$ and $\Delta pCO_{2\ simw}$ are the changes of pCO_2 by glacier meltwater and sea ice meltwater, respectively. $\Delta pCO_{2\ gmw+\ simw}$ is the total changes of pCO_2 by glacier meltwater and sea ice meltwater.

Figure 9 shows the pCO_2 and its change (ΔpCO_2) when mCDW on the TIS front was mixed with each water mass. The $pCO_{2\ gmw}$ when the mCDW flowing under the TIS was mixed with the basal meltwater was 440 ± 0.7 µatm ($\Delta pCO_{2\ gmw}$: –11 ± 0.6 µatm) in December 2019, 440 ± 0.2 µatm ($\Delta pCO_{2\ gmw}$: –11 ± 0.2 µatm) in March 2020, and

440 ± 0.6 μatm ($\Delta pCO_{2\ gmw}$: –11 ± 0.6 μatm) in March 2018 (Figures 9a, b). At the TIS front, the pCO_2 in seawater therefore decreased because of the dilution effect of the basal meltwater from the ice shelf. In addition, there were no seasonal changes between March and December or interannual changes between 2018 and 2020.

In contrast, the $pCO_{2\ simw}$ was 449 ± 1.5 μatm ($\Delta pCO_{2\ simw}$: –2 ± 1.5 μatm) when the mCDW was mixed with sea ice meltwater in December 2019 (Figures 9a, b). In contrast, the $pCO_{2\ simw}$ was 430 ± 0.3 μatm ($\Delta pCO_{2\ gmw}$: –21 ± 0.3 μatm) in March 2020, and 435 ± 0.7 μatm ($\Delta pCO_{2\ gmw}$: –16 ± 0.7 μatm) in March 2018 (Figures 9a, b). At the TIS front in March for both 2018 and 2020, the dilution effect of mixing with sea ice meltwater was greater than the dilution effect of mixing with ice shelf basal meltwater (Figures 9a, b). The pCO_2 therefore decreased because of mixing with sea ice meltwater in March, but the change of pCO_2 due to mixing with sea ice meltwater was small in December.

The $pCO_{2\ gmw+\ simw}$ when two meltwaters (sea ice meltwater, TIS basal meltwater) were mixed was 438 ± 1.4 μatm ($\Delta pCO_{2\ gmw}$: –13 ± 1.4 μatm) in December 2019, 418 ± 0.5 μatm ($\Delta pCO_{2\ gmw}$: –33 ± 0.5 μatm) in March 2020, and 424 ± 1.2 μatm ($\Delta pCO_{2\ mix}$: –27 ± 1.2 μatm) in March 2018 (Figures 9a, b). These results indicated that the TIS front reduced the pCO_2 in seawater because of the dilution effect of mixing with meltwater, but the seawater was supersaturated with respect to atmospheric pCO_2 (about 390 μatm). The dilution effect of TIS basal meltwater on the TIS front in March corresponded to a 2.4 ± 0.1% decrease of pCO_2, and the dilution effect of sea ice meltwater corresponded to a 4.1 ± 0.6% decrease. In contrast, the dilution effect of the basal meltwater from the Shirase Glacier Tongue calculated in Lützow-Holm Bay corresponded to a decrease of 9.6 ± 0.4% of pCO_2 (Kiuchi et al., 2021). In our study, the pCO_2 actually observed at the surface of each observation point ($pCO_{2\ obs}$) was 377 ± 46 μatm in December 2019, 246 ± 2.1 μatm in March 2020, and 232 ± 21 μatm in March 2018 (Figure 9a). Therefore, the pCO_2 was significantly decreased in the TIS front by other factors, especially photosynthesis of phytoplankton, in addition to the dilution effect of mixing with meltwater. In the following section, we discuss the effect of photosynthesis on the pCO_2 in the seawater.

4.2. Factors controlling the changes of DIC and TA at the ice front and coastal areas

In the ocean surface layer along the Antarctic coast in summer, the primary production by phytoplankton and the precipitation and dissolution of calcium carbonate ($CaCO_3 \cdot 6H_2O$) are known as important biological processes that affect the carbonate chemistry of the ocean (e.g., Legge et al., 2017; Shadwick et al., 2017; Arroyo et al., 2019). When DIC/TA changes due to photosynthesis by phytoplankton, the phytoplankton take up dissolved inorganic carbon (C) and nitrate (N) in the Redfield ratio (C:N = 106:16 by atoms) (Redfield et al., 1963). The ratio of the change of DIC to the change of TA is therefore 106:16 on a molar basis. In addition, when the ratio of DIC to TA changes because of the precipitation/dissolution of calcium carbonate, it changes in a ratio of DIC:TA = 1:2 (Zeebe and Wolf-Gladrow, 2001).

Figure 10 shows the relationship between nDIC and nTA, which was standardized to a salinity of 34.3, after the dilution effect of the meltwater was removed. Because the plot of the TIS front surface layer (0–100 dbar) did not follow the slope of nDIC:nTA = 1:2, the precipitation and dissolution of calcium carbonate were not the main effects on the carbonate chemistry of the surface layer along the Sabrina coast. This result was consistent with the observations made in the area from 31 December 2014 to 1 January 2015 (Arroyo et al., 2019). However, the fact that the plot followed the slope of nDIC:nTA = 106:16 indicates that the nDIC and nTA changed significantly due to photosynthesis of phytoplankton from the previous winter to summer. In addition, the nutrient concentrations in the surface layer in March (NO_3^-, PO_4^{3-}, and $Si(OH)_4$) were lower than those in the WW (Figure 6h–j). These results indicated that photosynthesis by phytoplankton occurred actively in the TIS front and the surrounding sea area in March, consuming DIC and nutrients in the seawater.

4.3. Net Community Production

To estimate the changes of DIC due to biological processes, net community production (NCP) was calculated using NO_3^- concentrations normalized to a salinity of 34.3 (nNO_3^-) (e.g., Shadwick et al., 2014). We defined NCP as the integrated change of the DIC concentrations at water depths of 20–100 m from winter to summer:

$$NCP = \left(\int_{z=20}^{z=100} [\mathrm{nN}]^{\mathrm{winter}} - [\mathrm{nN}]^{\mathrm{obs}}\, dz\right) \times 6.6 \qquad (11)$$

In Equation 11, z is the water depth, $[\mathrm{nN}]^{\mathrm{winter}}$ is the nNO_3^- concentration in winter, and $[\mathrm{nN}]^{\mathrm{obs}}$ is the nNO_3^- concentration at the time of observation. The temperature minimum layer is generally used to compare water masses in winter and summer (e.g., Bates et al., 1998; Ishii et al., 2002), but over the Antarctic continental shelf, it is difficult to define the temperature minimum layer (Murakami et al., 2020). Therefore, in this study, because the NO_3^- concentrations at a water depth of 200–300 dbar at the time of observation were vertically uniform at each observation (March 2018, December 2019, and March 2020), we averaged the NO_3^- concentrations (32.8 ± 0.4 μmol L^{-1} for March 2018, 31.1 ± 0.3 μmol L^{-1} for December 2019, and 31.2 ± 0.7 μmol L^{-1} for March 2020) and assumed that these were the NO_3^- concentrations at depths of 20–100 dbar in winter. NCP was converted to a carbon basis using the Redfield ratio (C:N = 106:16 by atoms) (Redfield et al., 1963). We then calculated NCP per day by assuming that photosynthesis by phytoplankton started on 1 November 2019 (e.g., Arroyo et al., 2019).

Figure 11 shows the NCP at the TIS front and coastal areas. The NCP for March 2018 was +28.7 ± 3.8 mmol m^{-2} day^{-1} (Figure 11a). It was particularly high in the western part of the study area (St. TT3: +35.9 mmol C m^{-2} day^{-1}) (Figure 11b). The March 2020 NCP was +39.9 ± 3.7 mmol m^{-2} day^{-1}, higher than the 2018 NCP at all stations (Figures 11a, c). The implication is that NCP changed over time, and there was more production

in March 2020. In contrast, the NCP for December 2019 was –1.6 ± 9.0 mmol C m^{-2} day^{-1} (Figure 11a). In particular, in the western part of the study area (Sts. TV 13, 15, 16, 17, and 19), the negative values of NCP indicated the predominance of respiration over photosynthesis. In the eastern part of the study area (Sts. TV20, 21, 22), NCP was positive (Figure 11d). A comparison of the NCP calculated in the same area from 31 December 2014 to 1 January 2015 (–3.8 to +6.6 mmol m^{-2} day^{-1}) (Arroyo et al., 2019) revealed that the December NCP calculated in this study was similar in magnitude, but the March NCP was comparatively very high (+39.9 ± 3.7 mmol m^{-2} day^{-1}).

We next used satellite images to compare the state of the ocean surface at each observation time. There was less sea ice in March than December (Figures 1b–d). Moreau et al. (2019) have reported that NCP is positively correlated with the proportion of sea ice meltwater. Figure 12a shows the relationship between the fractions of meltwater (F_{gmw}, F_{simw}) in the surface layer (20 dbar) and NCP. NCP was positively correlated with F_{simw}. This correlation is consistent with the results of Moreau et al. (2019) that higher F_{simw} results in higher NCP (Figure 12a). It appears that photosynthesis and NCP increased from December to March because the open water surface area was wider and the light environment was better due to the melting of sea ice. In addition, the relationship between the fractions of meltwater (F_{gmw}, F_{simw}) and NCP is shown only in the surface layer (20 dbar) in March 2018 and March 2020 (Figure 12b). Both F_{gmw} and F_{simw} were positively correlated with NCP, and the higher the fractions of meltwater, the higher the NCP tended to be. This result was likely due to stratification caused by the influence of the basal meltwater from the ice shelf and the melting of sea ice, the difference in the open water surface area, and a stable environment for the phytoplankton. It may also be affected by substances that promote phytoplankton growth, such as iron in basal meltwater and sea ice meltwater (Herraiz-Borreguero et al., 2016; Lannuzel et al., 2007). In section 4.4, we therefore assess the role of iron supplied by glacier basal meltwater by examining the ratios of nutrients taken up by phytoplankton.

4.4. Possibility of iron supply at TIS front

Primary production of Antarctic surface water is restricted mainly by iron (Martin et al., 1990; Moore et al., 2013). Sources of iron to the surface water are basal melting of ice shelves and subglacial discharged water (Arrigo et al., 2015; Herraiz-Borreguero et al., 2016), atmospheric dust (Jickells et al., 2005), vertical mixing in winter (Tagliabue et al., 2014), upwelling associated with fronts (Schallenberg et al. 2018), and melting of sea ice (Duprat et al., 2020; Lannuzel et al., 2007). Iron then stimulates primary production of the surface layer of the Southern Ocean. In general, the uptake ratio of nutrients by phytoplankton differs under iron-limited and iron-replete conditions; the Si/N and Si/P values are larger under iron-limited conditions than under iron-replete conditions (Takeda, 1998). To evaluate the presence or absence of iron supplied by meltwater in the TIS front surface layer (20 dbar), we therefore calculated the nutrient consumption ratios from winter to summer ($\Delta Si/\Delta N$, $\Delta Si/\Delta P$) using Equations 12 and 13 and the nutrient concentrations in the seawater:

$$\Delta Si/\Delta N = (Si_{WW} - nSi_{obs}) / (N_{WW} - nN_{obs}) \quad (12)$$

$$\Delta Si/\Delta P = (Si_{WW} - nSi_{obs}) / (P_{WW} - nP_{obs}) \quad (13)$$

In Equations 12 and 13, Si_{WW}, N_{WW}, and P_{WW} are the concentrations of each nutrient ($Si(OH)_4$, NO_3^-, PO_4^{3-}) contained in WW. The nSi_{obs}, nN_{obs}, and nP_{obs} are each nutrient concentration normalized to the salinity of WW (34.21 for March 2018, 34.18 for March 2020) in the surface layer (20 dbar) at the times of our observations. In addition, the average values of WW (64.0 ± 3.9 μmol L^{-1} for $Si(OH)_4$, 32.8 ± 0.4 μmol L^{-1} for NO_3^-, and 2.01 ± 0.04 μmol L^{-1} for PO_4^{3-} for March 2018, and 62.8 ± 4.3 μmol L^{-1} for $Si(OH)_4$, 31.2 ± 0.7 μmol L^{-1} for NO_3^-, and 2.16 ± 0.01 μmol L^{-1} for PO_4^{3-} for March 2020) were used as the nutrient concentrations in the surface layer in winter.

Figure 13 shows the ΔSi/ΔN and ΔSi/ΔP ratios at each observation point. In March 2018, ΔSi/ΔN and ΔSi/ΔP were low in the western part of the study area (Sts. TT2, 3) (ΔSi/ΔN = 1.2–1.3 mol mol^{-1}, ΔSi/ΔP = 23–25 mol mol^{-1}), but they were high in the eastern part of the study area (Sts. TT1, 4, 5, 6) (ΔSi/ΔN = 1.8–2.1 mol mol^{-1}, ΔSi/ΔP = 27–32 mol mol^{-1}). In March 2020, the ΔSi/ΔN and ΔSi/ΔP ratios were again low in the western part of the study area (St. TV34) (ΔSi/ΔN = 1.3 mol mol^{-1}, ΔSi/ΔP = 24 mol mol^{-1}) and higher in the eastern part of the study area (Sts. TV39, 40, 43) (ΔSi/ΔN = 1.5–1.6 mol mol^{-1}, ΔSi/ΔP = 26–27 mol mol^{-1}). These results indicate that the western part of the study area in March 2018 and 2020 was iron-replete and the eastern part of the study area in March 2018 was iron-limited in the surface water based on the analysis by Takeda (1998). Takeda (1998) has concluded that ΔSi/ΔN and ΔSi/ΔP ratios of 1.9–2.3 mol mol^{-1} and 16–42 mol mol^{-1}, respectively, are indicative of iron-limited conditions based on a culture experiment. We therefore defined ΔSi/ΔN ratios lower than 1.9–2.3 mol mol^{-1} and ΔSi/ΔP ratios less than 16–42 mol mol^{-1} as iron-replete conditions.

To evaluate the possibility of iron supply by meltwater, the relationship between ΔSi/ΔN, ΔSi/ΔP and the fractions of meltwater (F_{gmw}, F_{simw}) were examined (Figure 14). The ΔSi/ΔN and ΔSi/ΔP ratios were negatively correlated with the fractions of meltwater (F_{gmw}, F_{simw}). The higher the fractions of meltwater, the lower the ΔSi/ΔN and ΔSi/ΔP tended to be (Figure 14). In addition, as compared to F_{simw}, F_{gmw} were strongly correlated with ΔSi/ΔN and ΔSi/ΔP ratios. These results suggested that iron was supplied to the ocean surface by TIS basal meltwater rather than sea ice meltwater.

During March 2018, when observations were made on the west side of the TIS front, we found that there was an east-west gradient of the ΔSi/ΔN and ΔSi/ΔP ratios (Figures 13a, b). The ratios were low (iron-replete) on the west side and high (iron-limited) on the east side. The mCDW transport path that causes TIS basal melting transports mCDW from the outer edge of the continental shelf to the depression on the continental shelf because of factors such as eddies and seafloor topography (Hirano et al., 2021). The mCDW flows along the trough from the eastern side of the TIS (Rintoul et al., 2016; Silvano et al., 2017), where it causes melting, and then flows further westward.

The ocean current is considered to flow westward onto the shelf after exiting the cavity of TIS. Such circulation have also been observed in Lützow-Holm Bay, East Antarctica (Hirano et al., 2020; Kiuchi et al., 2021). These results suggest that primary production is promoted by the iron supplied by the glacial meltwater as it flows to the western flank of the TIS front.

The Amundsen Polynya and Pine Island Polynya, which are near the ice tongue/shelf off West Antarctica, are known to be areas of high productivity (Arrigo et al., 2015). It has been shown that the supply of iron to the surface layer of these polynyas following an influx of basal meltwater from the adjacent Pine Island Ice Shelf is an important factor that accounts for their high production rates (Gerringa et al., 2012). Likewise, the flow beneath the Pine Island Ice Shelf of the source water for the mCDW causes basal melting (Jacobs et al., 1996, 2011). It has been shown that in Prydz Bay, East Antarctica, the concentrations of dissolved iron and particulate iron are high in the marine ice that forms on the bottom of the Amery Ice Shelf. Melting of that marine ice supplies iron to the surface layer that is thought to account for the high productivity of the Mackenzie Polynya (Herraiz-Borreguero et al., 2016). Furthermore, Kanna et al. (2020) have shown that the iron input from a marine-terminating glacier in Greenland, which is supplied by a subglacial discharge plume, has the potential to fuel phytoplankton blooms in a glacial fjord.

Our study presents the first description of the potential supply of nutrients and iron to stimulate photosynthesis by phytoplankton in coastal Antarctic waters. The stimulation results from buoyancy-driven upwelling and mixing of nutrient-rich mCDW with iron-rich subglacial discharge and ice shelf basal meltwater (Figure 15). It is common knowledge that the supply of iron and nutrients plays an important role in allowing extensive phytoplankton blooms to develop in wind-driven coastal upwelling systems (Bruland et al., 2001; Fitzwater et al., 2003; Johnson et al., 1999). Likewise, near the ice front of the Antarctic coast, subglacial discharge and upwelling plumes supply abundant iron and macronutrients to the euphotic zone that sustains high productivity. Although we did not measure the iron concentrations in the water we sampled, a research project to examine the role of iron in Antarctic coastal waters is planned for future JARE

expeditions. That study will facilitate understanding of iron dynamics in not only the TIS system but also other Antarctic coastal waters because the rapid melting of ice shelves in recent years (e.g., Pritchard et al., 2012; Rignot et al., 2019) has provided huge amounts of freshwater to the coastal areas and high productivity was observed (e.g., Arrigo et al., 2015).

5. Conclusions

Hydrographic observations were conducted from the continental shelf slopes of the Sabrina Coast to the TIS front from December to March of 2018, 2019, and 2020. The mCDW, a water mass with relatively high temperature and high salinity, was transported from the outer edge of the continental shelf into a depression on the shelf and then flowed into the deep layers of the TIS along a trough to supply heat and biogeochemical components. At the TIS front, biogeochemical components changed significantly due to the mixing of mCDW with meltwater from sea ice and TIS basal meltwater. In addition to mixing/dilution effects, the surface layer was strongly influenced by biological activity, especially photosynthesis by phytoplankton. During the entire observation period, the pCO_2 in seawater was reduced by mixing with TIS basal meltwater and sea ice meltwater at the TIS front and in the surrounding surface layer. The dilution effect of mixing TIS with basal meltwater corresponded to a 2.4–2.6% reduction of the pCO_2 in seawater over the entire observation period. The dilution effect of mixing with sea ice meltwater was small in December, but in March it exceeded the dilution effect of mixing TIS with basal meltwater and corresponded to a 3.6–4.8% decrease of salinity. In March, as the open water surface area expanded due to the melting of sea ice, pCO_2 decreased significantly due to photosynthesis by phytoplankton, and the pCO_2 in seawater was undersaturated with respect to the atmosphere. The ratios of nutrients taken up by phytoplankton indicated that iron contained in the basal meltwater of the TIS may have helped to stimulate photosynthesis by phytoplankton, especially on the west side of the TIS front.

Acknowledgments

We thank the crews of R/V *Kaiyo-maru* and icebreaker *Shirase* as well as participants in the cruises for their support in conducting the field work, especially Tomohide Noguchi. We also thank Megumi Kitagawa for oxygen isotopic ratio analyses. We benefited greatly from the advice offered by Atsushi Ooki and from his useful comments concerning the carbonate chemistry and nutrient data in this paper. This work was supported by grants from the Japan Society for the Promotion of Science (#17H04715, #17H04710, #17H06317, #17H06322, #17K12811, #20K12132, #20H04345, #21H04931, #21H0491, #20H04961, and #20K12132), the Science Program of the Japanese Antarctic Research Expedition (JARE) as Prioritized Research AJ0902 (ROBOTICA), the National Institute of Polar Research (NIPR) through Project Research KP-303 and General Collaboration Project #28-14, #2-13, and a grant for education of young scientists, the Center for the Promotion of Integrated Sciences of SOKENDAI, and the Joint Research Program of the Institute of Low Temperature Science, Hokkaido University. The data used in the study are available in the supporting information (Table S1). Data archiving in the data repository of the National Institute of Polar Research, Tokyo, Japan, is underway.

References

Arrigo, K. R., van Dijken, G. L., & Strong, A. L. (2015). Environmental controls of marine productivity hot spots around Antarctica. *Journal of Geophysical Research: Oceans, 120*, 5545–5565. https://doi.org/10.1002/2015JC010888

Arroyo, M. C., Shadwick E. H., & Tilbrook, B. (2019). Summer Carbonate Chemistry in the Dalton Polynya, East Antarctica. *Journal of Geophysical Research: Oceans, 124*, 1–20. https://doi.org/ 10.1029/2018JC014882

Bates, N. R., Hansell, D. A., & Carlson, C. A. (1998). Distribution of CO_2 species, estimates of net community production, and air-sea CO_2 exchange in the Ross Sea polynya. *Journal of Geophysical Research: Oceans, 103*, 2883–2896. https://doi.org/10.1029/97JC02473

Bruland, K. W., Rue, E. L., & Smith, G. J. (2001). Iron and macronutrients in California coastal upwelling regimes: Implications for diatom blooms. *Limnology and Oceanography, 46*, 1661–1674. https://doi.org/10.4319/lo.2001.46.7.1661

de Baar, H. J. W., Buma, A. G. J., Nolting, R. F., Cadée, G. C., Jacques, G., & Tréguer, P. J. (1990). On iron limitation of the Southern Ocean: Experimental observations in the Weddell and Scotia Seas. *Mar. Ecol. Prog. Ser.*, 65, 105–122.

Dickson, A. G. (1990). Thermodynamics of the dissociation of boric acid in synthetic seawater from 273.15 to 318.15 K. *Deep-Sea Research Part I: Oceanographic Research Papers, 37*, 755–766.

Dickson, A. G., & Millero, F. J. (1987). A comparison of the equilibrium constants for the dissociation of carbonic acid in seawater media. *Deep-Sea Research Part A: Oceanographic Research Papers, 34*, 1733–1743.

Dickson, A. G., Sabine, C. L., & Christian, J. R. (Eds.) (2007). *Guide to best practices for ocean CO_2 measurement, PICES Special Publication 3*. Sidney, B.C., Canada: North Pacific Marine Science Organization.

Duprat, L., Corkill, M., Genovese, C., Townsend, A. T., Moreau, S., Meiners, K. M., et al. (2020). Nutrient distribution in east Antarctic summer sea ice: A potential iron contribution from glacial basal melt. *Journal of Geophysical Research: Oceans*, 125, 12. DOI: http://dx.doi.org/10.1029/2020jc016130

Fitzwater, S. E., Johnson, K. S., Elrod, V. A., Ryan, P., Coletti, L. J., Tanner, S. J., et al. (2003). Iron, nutrient and phytoplankton biomass relationships in upwelled waters of the

California coastal system. *Continental Shelf Research*, *23*, 16, 1523–1544. https://doi.org/10.1016/j.csr.2003.08.004

Gerringa, L. J., Alderkamp, A. C., Laan, P., Thuróczy, C. E., de Baar, H. J., Mills, M. M., et al. (2012). Iron from melting glaciers fuels the phytoplankton blooms in Amundsen Sea (Southern Ocean): Iron biogeochemistry. *Deep-Sea Research Part II: Topical Studies in Oceanography*, 71–76, 16–31. https://doi.org/10.1016/j.dsr2.2012.03.007

Greenbaum, J. S., Blankenship, D. D., Young, D. A., Richter, T. G., Roberts, J. L., Aitken, A. R. A., et al. (2015). Ocean access to a cavity beneath Totten Glacier in East Antarctica. *Nature Geoscience, 8*, 4, 294–298. https://doi.org/10.1038/ ngeo2388

Herraiz-Borreguero, L., Lannuzel, D., van der Merwe, P., Treverrow, A., & Pedro, J. B. (2016). Large flux of iron from the Amery Ice Shelf marine ice to Prydz Bay, East Antarctica. *Journal of Geophysical Research: Oceans, 121*, 6009–6020. https://doi.org/10.1002/ 2016JC011687

Hirano, D., Tamura, T., Kusahara, K., Ohshima, K. I., Nicholls, K. W., Ushio, S., et al. (2020). Strong ice-ocean interaction beneath Shirase Glacier Tongue in East Antarctica. *Nature Communications, 11*, 4421. https://doi.org/10.1038/s41467-020-17527-4

Hirano, D., Mizobata, K., Sasaki, H., Murase, H., Tamura, T., & Aoki, S. (2021). Poleward eddy-induced warm water transport across a shelf break off Totten Ice Shelf, East Antarctica. *Communications Earth & Environment, 2*, 153. https://doi.org/10.1038/s43247-021-00217-4

Ishi, M., Inoue, H. Y., & Matsueda, H. (2002), Net community production in the marginal ice zone and its importance for the variability of the oceanic pCO_2 in the Southern Ocean south of Australia. *Deep Sea Research, Part II, 49*, 1691–1706. https://doi.org/10.1016/S0967-0645(02)00007-3

Jacobs, S. S., Hellmer, H. H., & Jenkins, A. (1996). Antarctic ice sheet melting in the southeast Pacific. *Geophysical Research Letters, 23*, 957–960. https://doi.org/10.1029/96GL00723

Jacobs, S. S., Jenkins, A., Giulivi, C. F., & Dutrieux, P. (2011). Stronger ocean circulation and increased melting under Pine Island Glacier ice shelf. *Nature Geoscience, 4*, 8, 519–523. https://doi:10.1038/ngeo1188

JGOFS (1994). *Protocols for the Joint Global Ocean Flux Study core measurements. International JGOFS Report Series, vol. 19*. Bergen, Norway: JGOFS International Project Office.

Jickells, T. D., An, Z. S., Andersen, K. K., Baker, A. R., Bergametti, G., Brooks, N., et al. (2005). Global Iron Connections Between Desert Dust, Ocean Biogeochemistry, and Climate. *Science, 308*, 5718, 67–71. https://doi.org/10.1126/science.1105959

Johnson, K. M., King, A. E., & Sieburth, J. M. (1985). Coulometric TCO_2 analyses for marine studies: An introduction. *Marine Chemistry, 16*, 61–82.

Johnson, K. M. (1992). Single-Operator Multiparameter Metabolic Analyzer (SOMMA) for Total Carbon Dioxide (CT) with Coulometric Detection. *SOMMA Manual 1.0*, January 1992, Brookhaven National Laboratory, 70 pp.

Johnson, K. S., Chavez, F. P., & Friederich, G. E. (1999). Continental-shelf sediment as a primary source of iron for coastal phytoplankton. *Nature, 398*, 697–700. https://doi.org/10.1038/19511

Kanna, N., Sugiyama, S., Fukamachi, Y., Nomura, D., & Nishioka, J. (2020). Iron supply by subglacial discharge into a fjord near the front of a marineterminating glacier in northwestern Greenland. *Global Biogeochemical Cycles, 34*, e2020GB006567. https://doi.org/10.1029/2020GB006567

Kiuchi, M., Nomura, D., Hirano, D., Tamura, T., Hashida, G., Ushio, S., et al. (2021). The effect of basal melting of the Shirase Glacier Tongue on the CO_2 system in Lützow-Holm Bay, East Antarctica. *Journal of Geophysical Research: Biogeosciences, 126*, e2020JG005762. https://doi.org/10.1029/2020JG005762

Lannuzel, D., Schoeman, V., de Jong, J., Tison, J., & Chou, L. (2007). Distribution and biogeochemical behaviour of iron in the East Antarctic sea ice. *Marine Chemistry 106*, 18–32. https://doi.org/10.1016/j.marchem.2006.06.010

Legge, O. J., Bakker, D. C., Meredith, M. P., Venables, H. J., Brown, P. J., Jones, E. M., et al. (2017). The seasonal cycle of carbonate system processes in Ryder Bay, West Antarctic Peninsula. *Deep-Sea Research Part II: Topical Studies in Oceanography, 139*, 167–180. https://doi.org/10.1016/j.dsr2.2016.11.006

Lenton, A., Tilbrook, B., Law, R., Bakker, D. C. E., Doney, S. C., Gruber, N., et al. (2013). Sea–air CO_2 fluxes in the Southern Ocean for the period 1990–2009. *Biogeosciences, 10*, 4037–4054. https://doi.org/10.5194/bg-10-4037-2013

Lewis, E. L. & Perkin, R. G. (1986). Ice Pump and Their Rates. *Journal of geophysical Research, 91, 10*, 11756–11762. https://doi.org/10.1029/JC091iC10p11756

Li, X., Rignot, E., Morlighem, M., Mouginot, J., & Scheuchl, B. (2015). Grounding line retreat of Totten Glacier, East Antarctica, 1996 to 2013, *Geophys. Res. Lett.*, 42, 8049–8056, doi:10.1002/2015GL065701

Martin J. H. (1990). Glacial-Interglacial CO_2 change: the iron hypothesis, *Paleoceanography, 5, 1*, 1–13. https://doi.org/10.1029/PA005i001p00001

Mehrbach, C., Culberson, C. H., Hawley, J. E., & Pytkowicz, R. M. (1973). Measurement of the apparent dissociation constants of carbonic acid in seawater at atmospheric pressure. *Limnology and Oceanography, 18*, 6, 897–907.

Meredith, M. P., Brandon, M. A., Wallace, M. I., Clarke, A., Leng, M. J., Renfrew, I. A., et al. (2008). Variability in the freshwater balance of northern Marguerite Bay, Antarctic Peninsula: Results from $\delta^{18}O$. *Deep-Sea Research Part II: Topical Studies in Oceanography, 55,* 3–4, 309–322. https://doi.org/10.1016/j.dsr2.2007.11.005

Moore, C. M., Mills, M. M., Arrigo, K. R., Berman-Frank, I., Bopp, L., Boyd, P. W., et al. (2013). Processes and patterns of oceanic nutrient limitation. *Nature Geoscience, 6*, 9, 701–710. https://doi.org/10.1038/ngeo1765

Moreau, S., Lannuzel, J., Janssens, J., Arroyo, M. C., Corkill, E., Cougnon, C., et al. (2019). Sea Ice Meltwater and Circumpolar Deep Water Drive Contrasting Productivity in Three Antarctic Polynya. *Journal of Geophysical Research: Oceans, 124, 5*, 2943–2968. https://doi.org/10.1029/2019JC015071

Murakami, K., Nomura, D., Hashida, G., Nakaoka, S., Kitade, Y., Hirano, D., et al. (2020). Strong biological carbon uptake and carbonate chemistry associated with dense shelf water outflows in the Cape Darnley polynya, East Antarctica. *Marine Chemistry, 225*, 103842. https://doi.org/10.1016/j.marchem.2020.103842

Nitsche F. O., Porter, D., Williams, G., Cougnon, E. A., Fraser, A. D., Correia, R., et al. (2017). Bathymetric control of warm ocean water access along the East Antarctic Margin. *Geophysical Research Letters, 44, 17*, 8936–8944. https://doi.org/10.1002/2017GL074433

Oliver, H., St-Laurent, P., Sherrell, R. M., & Yager, P. L. (2019). Modeling iron and light controls on the summer Phaeocystis antarctica bloom in the Amundsen Sea Polynya. *Global Biogeochemical Cycles, 33*, 570–596. https://doi.org/10.1029/2018GB006168

Ono, T., Watanabe S., Okuda, K., & Fukasawa, M. (1998). Distribution of total carbonate and related properties in the North Pacific along 30°N. *Journal of*

Geophysical Research: Oceans, 103, C13, 30873–30883.

Orr, J. C., Epitalon, J.-M., Dickson, A. G., & Gattuso, J.-P. (2018). Routine uncertainty propagation for the marine carbon dioxide system. *Marine Chemistry, 207*, 84–107. https://doi.org/10.1016/j.marchem.2018.10.006

Parsons, T. R., Takahashi, M., & Hargrave, B. (1984). *Biological oceanographic processes* (3rd ed.). Oxford, UK: Pergamon.

Pritchard, H., Ligtenberg, S., Fricker, H., Vaughan, D. G., van den Broeke, M. R., & Padman, L. (2012). Antarctic ice-sheet loss driven by basal melting of ice shelves. *Nature, 484*, 502–505. https://doi.org/10.1038/nature10968

Redfield, A. C., Ketchum, B. H., and Richards, F. A. (1963). The influence of organisms on the composition of sea water. In: Hill, M. (Ed.), The Sea. John Wiley & Sons, New York, vol. 2, 26–77.

Rignot, E., Mouginot, J., Scheuchl, B., van den Broeke, M., van Wessem, M. J., & Morlighem, M. (2019). Four decades of Antarctic Ice Sheet mass balance from 1979–2017. *Proceedings of the National Academy of Sciences*, *116*, 4, 1095–1103. DOI: 10.1073/pnas.1812883116

Rintoul, S. R., Silvano, A., Pena-Molino, B., van Wijk, E., Rosenberg, M., Greenbaum, J. S., et al. (2016). Ocean heart drives rapid basal melt of the Totten Ice Shelf. *Science Advances, 16, 2, 12*, 1601–1610. https://doi.org/10.1126/sciadv.1601610

Schallenberg, C., Bestley, S., Klocker, A., Trull, T. W., Davies, D. M., Gault-Ringold, M., et al. (2018). Sustained upwelling of subsurface iron supplies seasonally persistent phytoplankton blooms around the southern Kerguelen plateau, Southern Ocean. *Journal of Geophysical Research: Oceans,* 123, 8, 5986–6003. https://doi.org/10.1029/2018JC013932

Shadwick, E. H., Tilbrool, B., & Williams, G. D. (2014). Carbonate chemistry in the Mertz Polynya (East Antarctica): Biological and physical modification of dense water outflows and the export of anthropogenic CO_2. *Journal of Geophysical Research: Oceans, 119, 1*, 1–14. https://doi.org/10.1002/2013JC009286

Shadwick, E. H., Tilbrook, B., & Currie, K. I. (2017). Late-summer biogeochemistry in the Mertz Polynya: East Antarctica. *Journal of Geophysical Research: Oceans, 122*, 7380–7394. https://doi.org/10.1002/2017JC013015

Silvano, A., Rintoul, S. R., Pena-Molino, B., & Williams, G. D. (2017). Distribution of water masses and meltwater on the continental shelf near the Totten and Moscow University ice shelves. *Journal of Geophysical Research: Oceans, 122*, 2050–2068. https://doi.org/10.1002/2016JC012115

Silvano, A., Rintoul, S. R., Peña-Molino, B., Hobbs, W. R., van Wijk, E., Aoki, S., et al. (2018). Freshening by glacial meltwater enhances melting of ice shelves and reduces formation of Antarctic Bottom Water. *Science Advances, 4*, 4, eaap9467. https://doi.org/10.1126/ sciadv.aap9467

Silvano, A., Rintoul, S. R., Kusahara, K., Pena-Molino, B., van Wijk, E., Gwyther, D. E., et al. (2019). Seasonality of Warm Water Intrusions Onto the Continental Shelf Near the Totten Glacier. *Journal of Geophysical Research: Oceans, 124, 6*, 4272–4289. https://doi.org/10.1029/2018JC014634

St-Laurent, P., Yager, P. L., Sherrell, R. M., Oliver, H., Dinniman, M. S., & Stammerjohn, S. E. (2019). Modeling the seasonal cycle of iron and carbon fluxes in the Amundsen Sea Polynya, Antarctica. *Journal Geophysical Research: Oceans, 124*, 1544–1565. https://doi.org/10.1029/2018JC014773

Suzuki, R., & Ishimaru, T. (1990). An improved method for the determination of phytoplankton chlorophyll using *N,N*-dimethylformamide. *Journal of the Oceanographic Society of Japan, 46*, 190–194. https://doi.org/10.1007/BF02125580

Tagliabue, A., Sallee, J., Bowie, A., Levy, M., Swart, S. & Boyd, P. W. (2014). Surface-water iron supplies in the Southern Ocean sustained by deep winter mixing. *Nature Geoscience, 7*, 314–320. https://doi.org/10.1038/ngeo2101

Takahashi, T., Sweeney, C., Hales, B., Chipman, D., Newberger, T., Goddard, J., et al (2012). The changing carbon cycle in the Southern Ocean. *Oceanography, 25*, 3, 26–37. http://www.jstor.org/stable/24861390

Takeda, S. (1998). Influence of iron availability on nutrient consumption ratio of diatoms in oceanic waters. *Nature, 393*, 774–777. https://doi.org/10.1038/31674

Tamura, T., Ohshima, K. I., & Nihashi, S. (2008). Mapping of sea ice production for Antarctic coastal polynyas. *Geophysical Search Letters, 35*, L07606. doi:10.1029/2007GL032903

Zeebe, R. E., & Wolf-Gladrow, D. A. (2001). CO_2 in seawater: equilibrium, kinetics, isotopes. *Elsevier Oceanography Series volume 65*, Amsterdam, the Netherlands: Elsevier.

Figure Captions

Figure 1. (a) CTD stations from offshore slope to Totten Ice Shelf (TIS) front in Sabrina Coast, East Antarctica during spring/summer 2018, 2019, and 2020. MODIS-Terra satellite images from March 2018. (b) CTD stations at TIS front in March 2018. MODIS-Terra satellite images from March 2018. (c) CTD stations at TIS front in December 2019. MODIS-Terra satellite images from December 2019. (d) CTD stations at TIS front in March 2020. MODIS-Terra satellite images from March 2020.

Figure 2. Vertical sections of (a) temperature, (b) salinity, (c) DIC, (d) TA, (e) NO_3^-, (f) PO_4^{3-}, and (g) $Si(OH)_4$ along the continental shelf. (h) CTD stations and MODIS-Terra

satellite images from February 2019.

Figure 3. Vertical sections of (a) temperature, (b) salinity, (c) DIC, (d) TA, (e) NO_3^-, (f) PO_4^{3-}, and (g) $Si(OH)_4$ at TIS front in March 2018. (h) CTD stations and MODIS-Terra satellite images from March 2018.

Figure 4. Vertical sections of (a) temperature, (b) salinity, (c) DIC, (d) TA, (e) NO_3^-, (f) PO_4^{3-}, and (g) $Si(OH)_4$ at TIS front in March 2020. (h) CTD stations and MODIS-Terra satellite images from March 2020.

Figure 5. Vertical sections of (a) temperature, (b) salinity, (c) DIC, (d) TA, (e) NO_3^-, (f) PO_4^{3-}, and (g) $Si(OH)_4$ at TIS front in December 2019. (h) CTD stations and MODIS-Terra satellite images from December 2019.

Figure 6. Vertical profiles of (a) temperature, (b) salinity, (c) DIC, (d) TA, (e) nDIC, (f) nTA, (g) $\delta^{18}O$, (h) NO_3^-, (i) PO_4^{3-}, and (j) $Si(OH)_4$ at TIS front. Mean values for March 2018 (red), December 2019 (green), and March 2020 (orange), and for all stations (gray).

Figure 7. Vertical sections of (a) temperature, (b) salinity, (c) DIC, (d) TA, (e) NO_3^-, (f) PO_4^{3-}, (g) $Si(OH)_4$ from offshore slope to TIS front (Sts. TT1–6, TV34, TV39, TV83, TV85, TV86, TV101, 517–521. (h) MODIS-Terra satellite images from March 2018.

Figure 8. Vertical profiles of (a) F_{gmw}, (b) F_{simw}, and (c) F_{mCDW} at TIS front. Mean values for March 2018 (red), December 2019 (green), and March 2020 (orange), and for all stations (gray). Spatial distribution of F_{gmw} and F_{simw} in surface water (20 dbar) for March 2018 (red) (d, g), December 2019 (green) (e, h), and March 2020 (orange) (f, i).

Figure 9. The pCO_2 (a) and the amount of change (ΔpCO_2) (b) when mCDW at the TIS ice front is mixed with each water mass.

Figure 10. Relationships between nDIC and nTA for depths <100 dbar in December

2019 (green), <100 dbar in March 2020 (yellow), <100 dbar in March 2018, and >100 dbar for all stations (gray). Dashed lines indicate photosynthesis or respiration (green line, slope = −0.15), the precipitation or dissolution of calcium carbonate (red line, slope = 2.0) and CO_2 exchange (blue line, slope = 0).

Figure 11. NCP for (a) December 2019 (green) and March 2020 (yellow) and spatial distribution of NCP for (b) March 2018, (c) March 2020, and (d) December 2019.

Figure 12. Relationship between NCP, F_{gmw}, and F_{simw} for (a) December 2019 and March 2018 and 2020 and (b) March 2018 and 2020.

Figure 13. Spatial distribution of ΔSi/ΔN for (a) March 2018 and (b) March 2020, and ΔSi/ΔP for (c) March 2018 and (d) March 2020.

Figure 14. Relationship between fractions of glacier meltwater (F_{gmw}) and sea ice meltwater (F_{simw}) and (a) ΔSi/ΔN and (b) ΔSi/ΔP at the TIS front in March 2018 and 2020.

Figure 15. Schematic illustration of the TIS nutrient and iron supply system from the bottom of the TIS to the surface of the ocean near the ice front

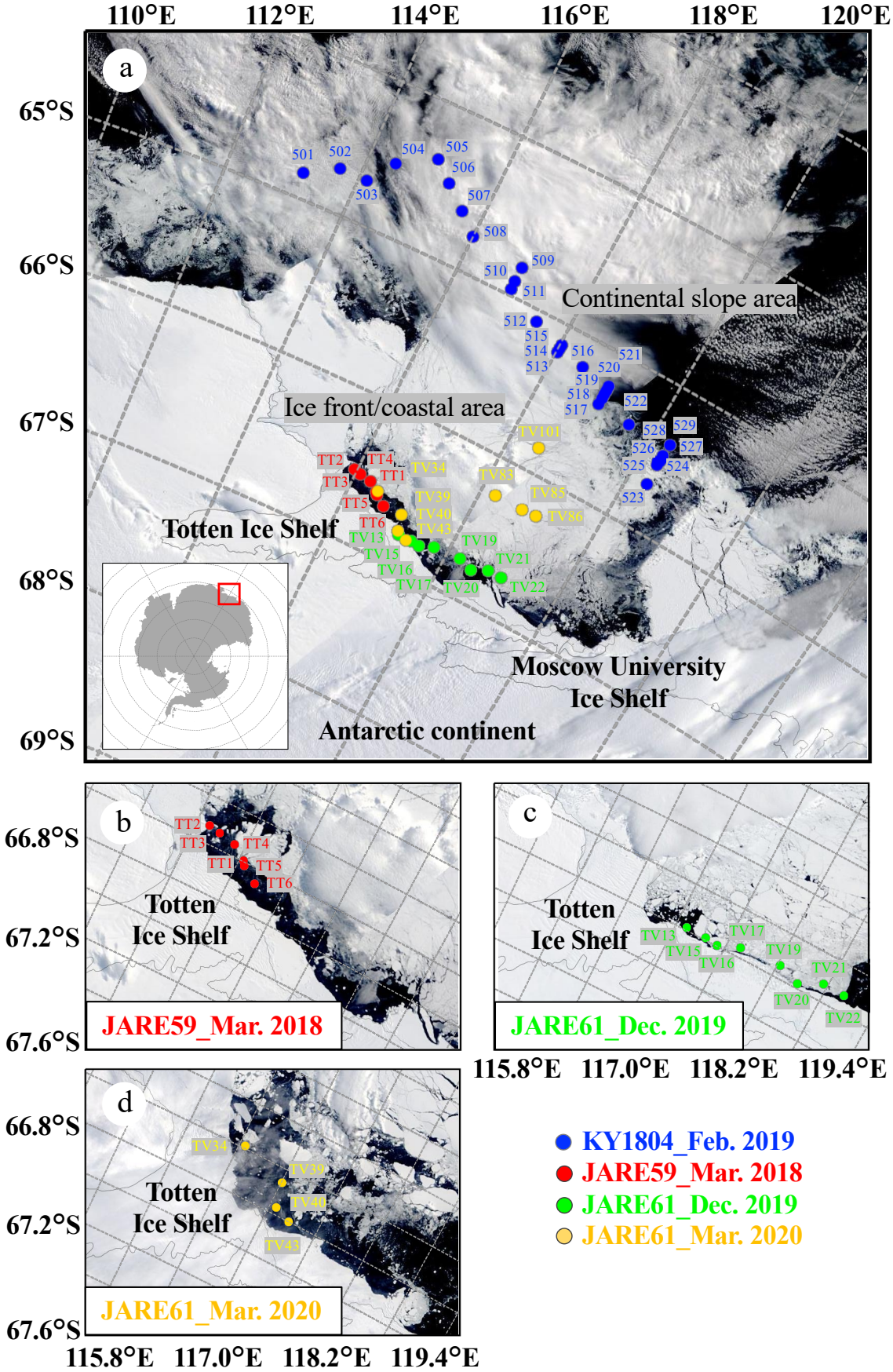

Figure 1_Tamura et al.

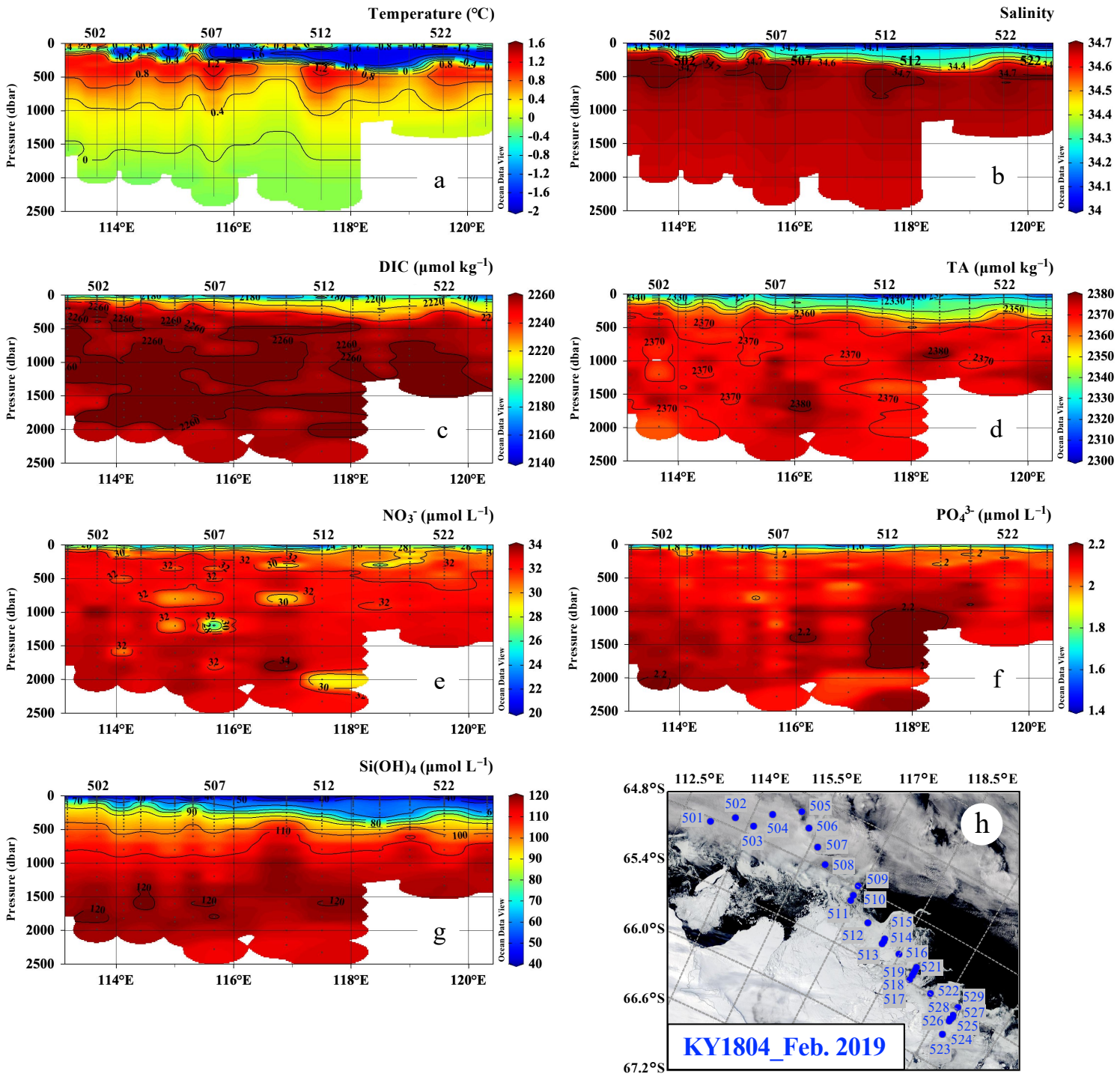

Figure 2_Tamura et al.

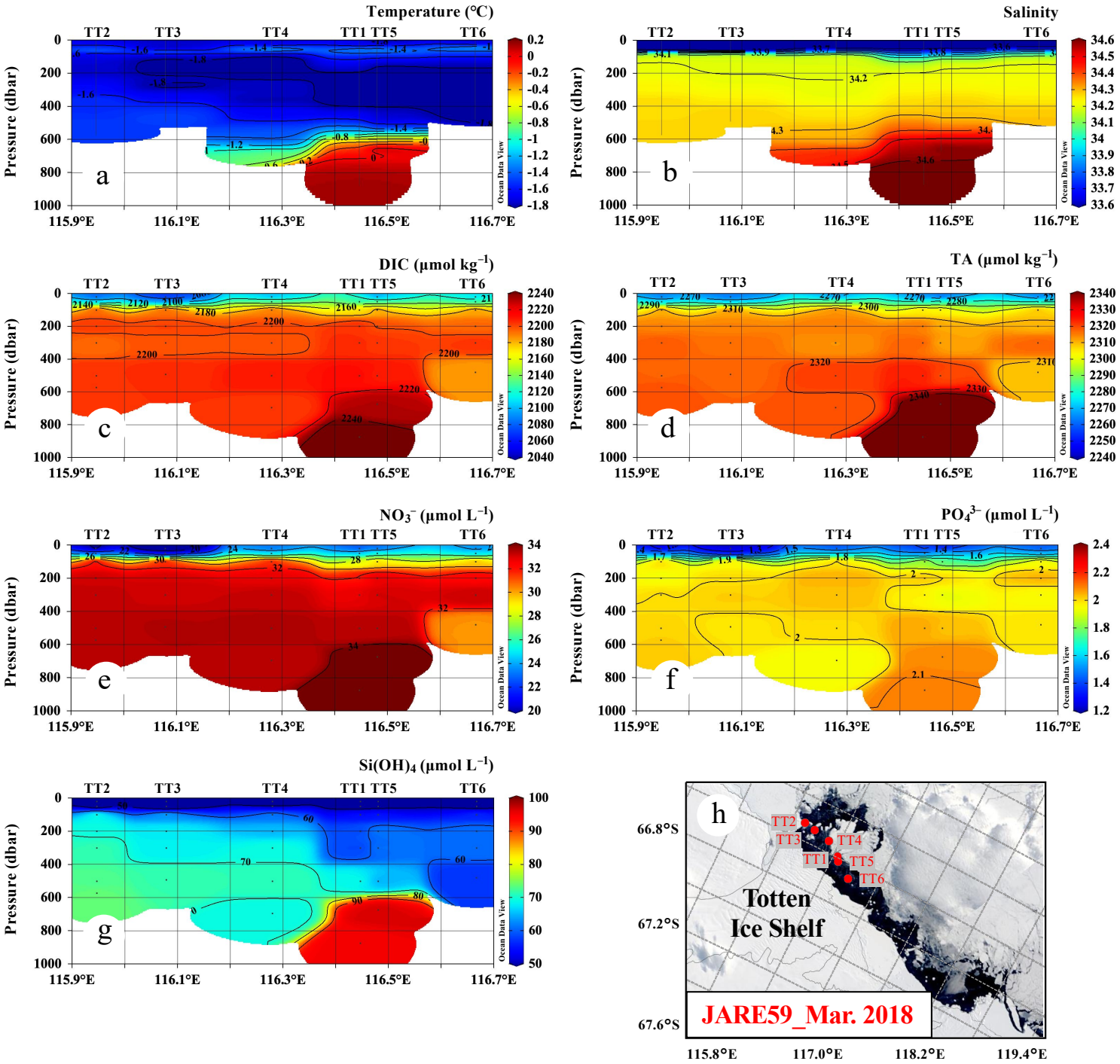

Figure 3_Tamura et al.

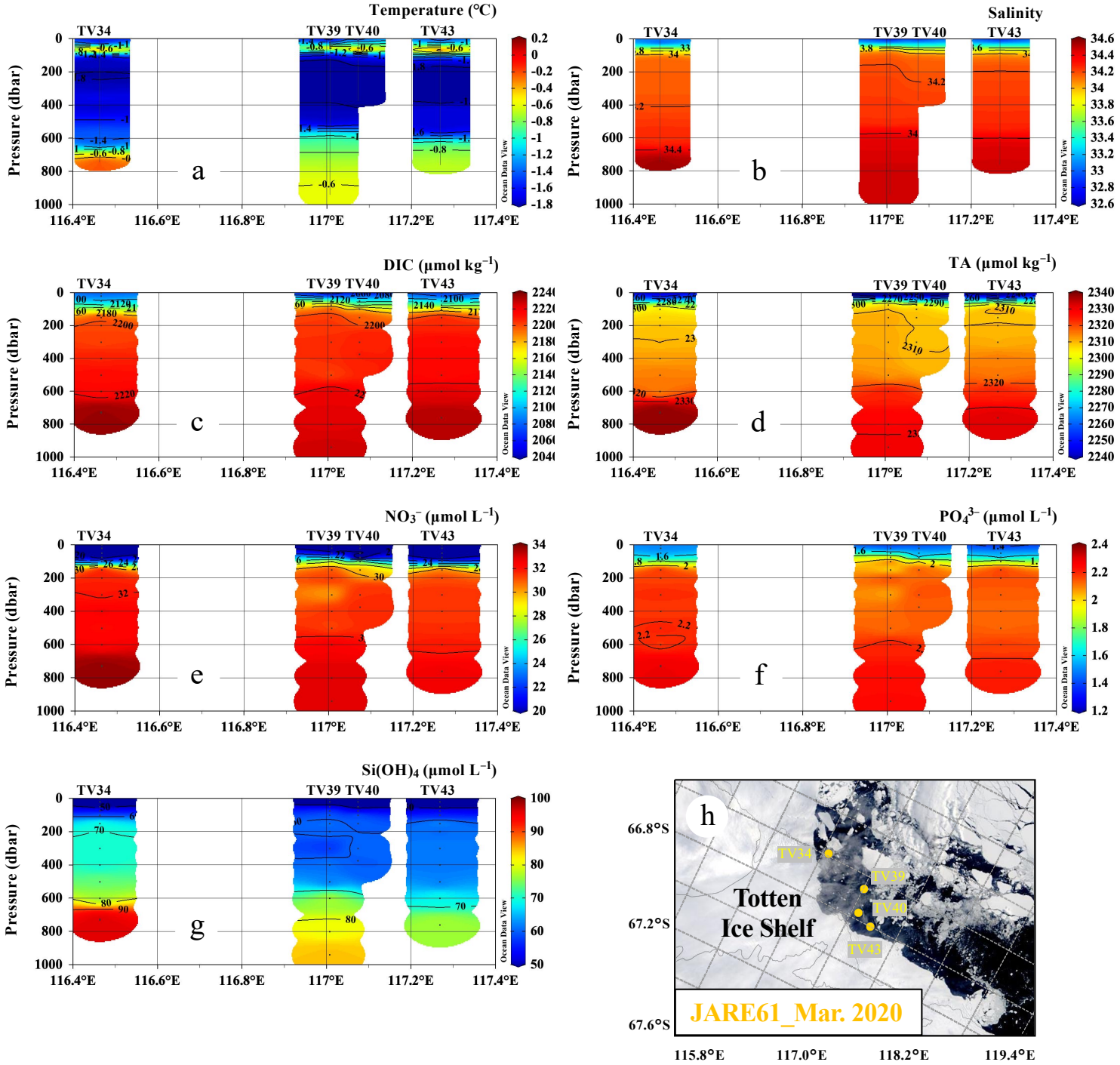

Figure 4_Tamura et al.

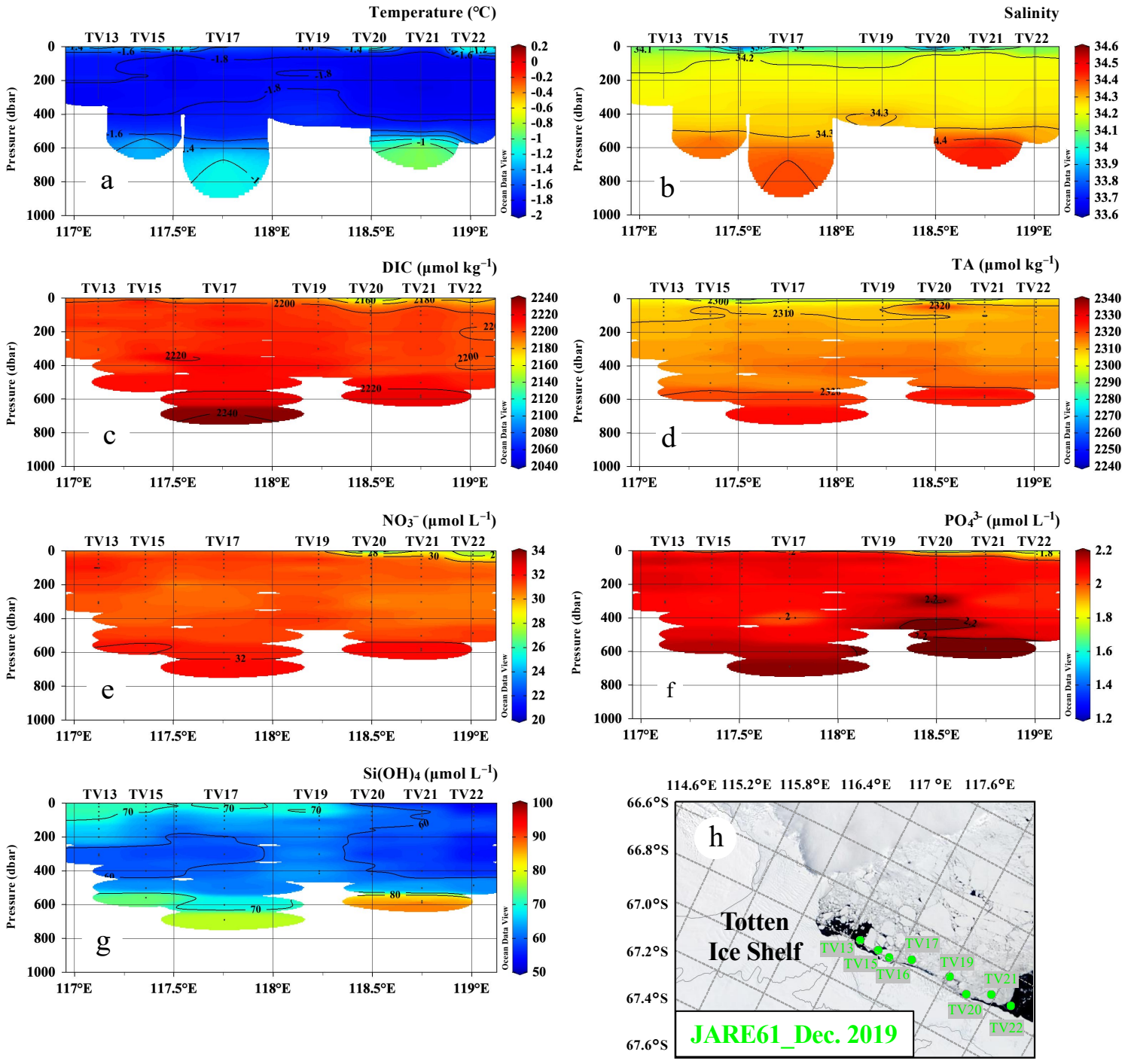

Figure 5_Tamura et al.

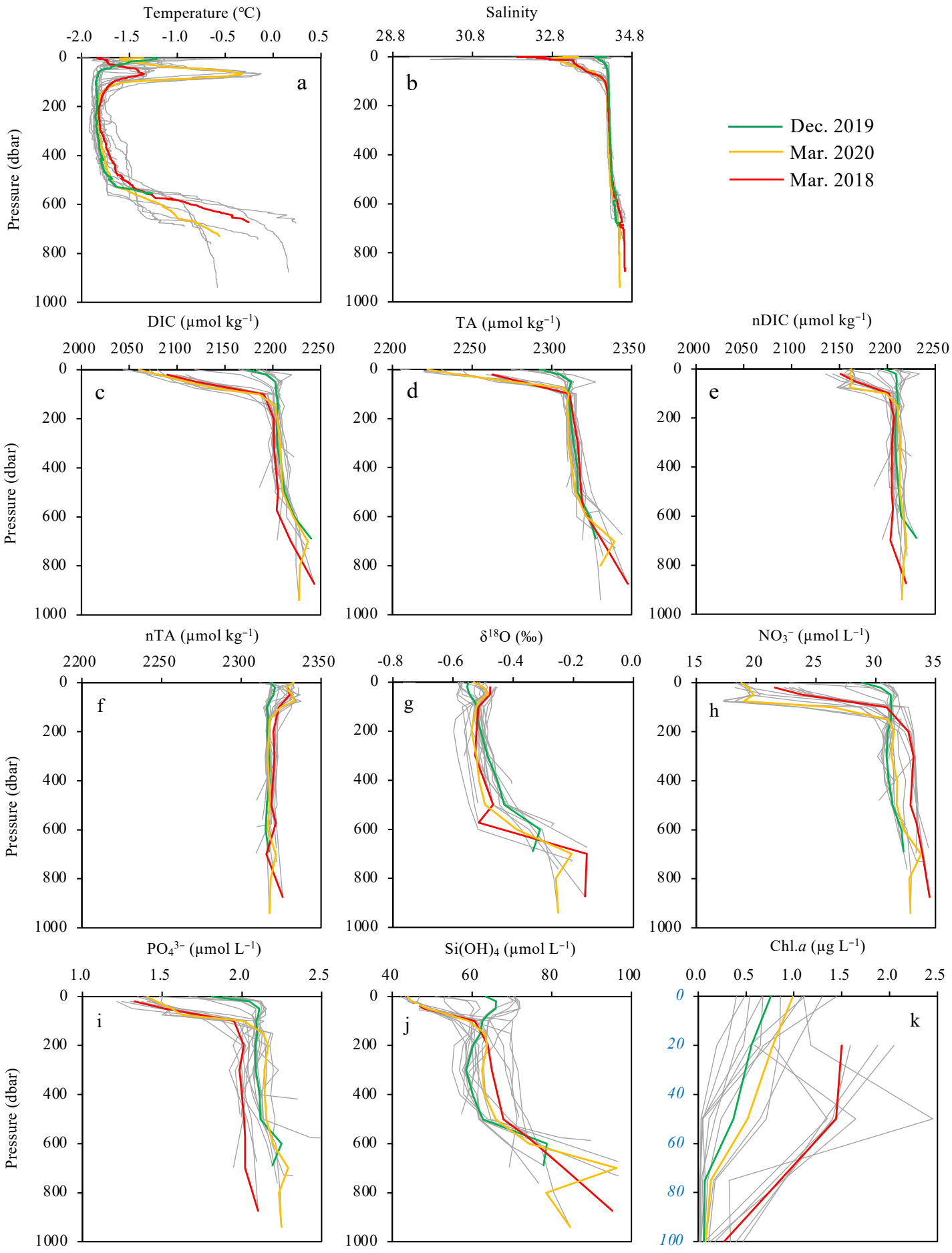

Figure 6_Tamura et al.

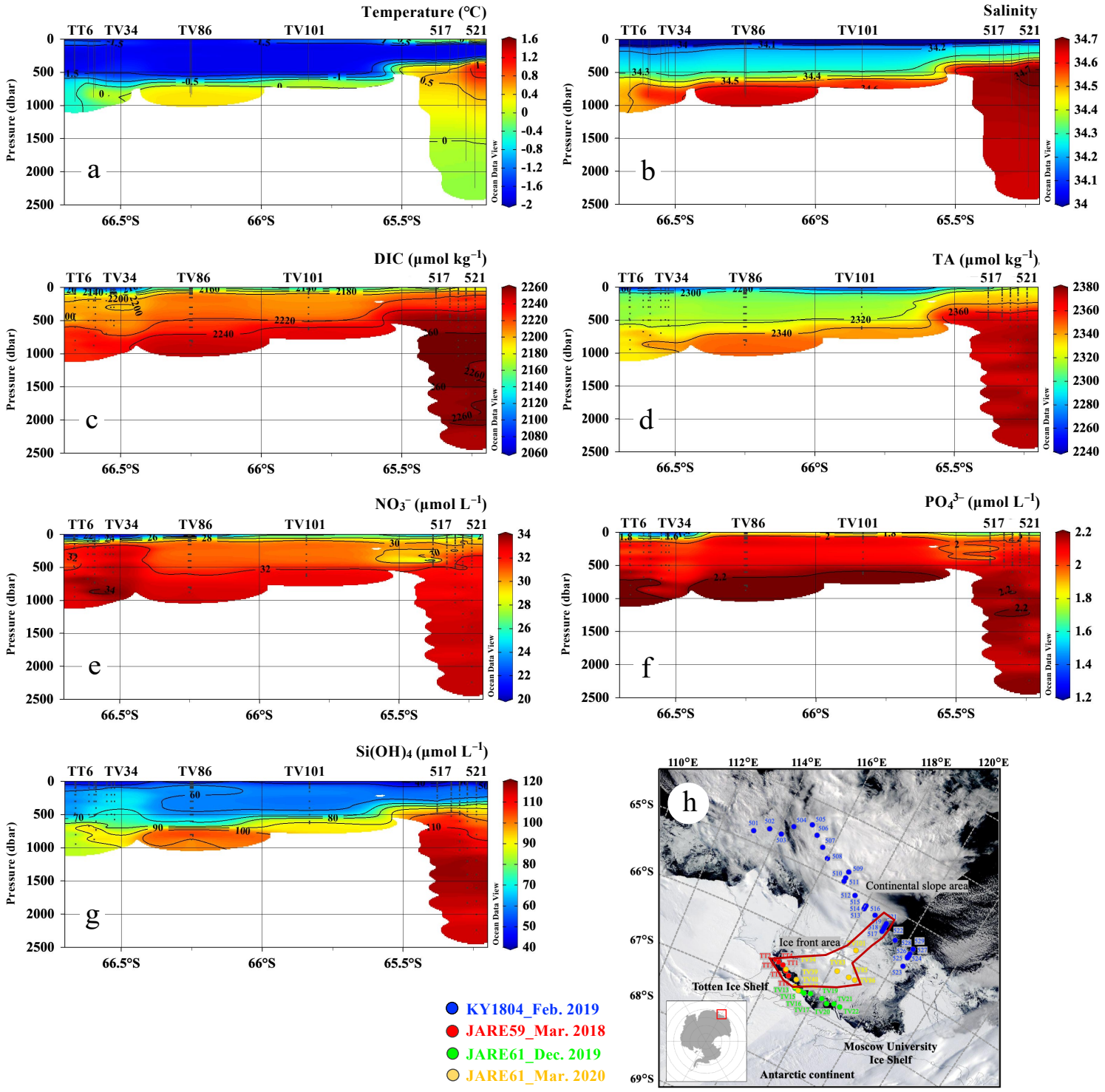

Figure 7_Tamura et al.

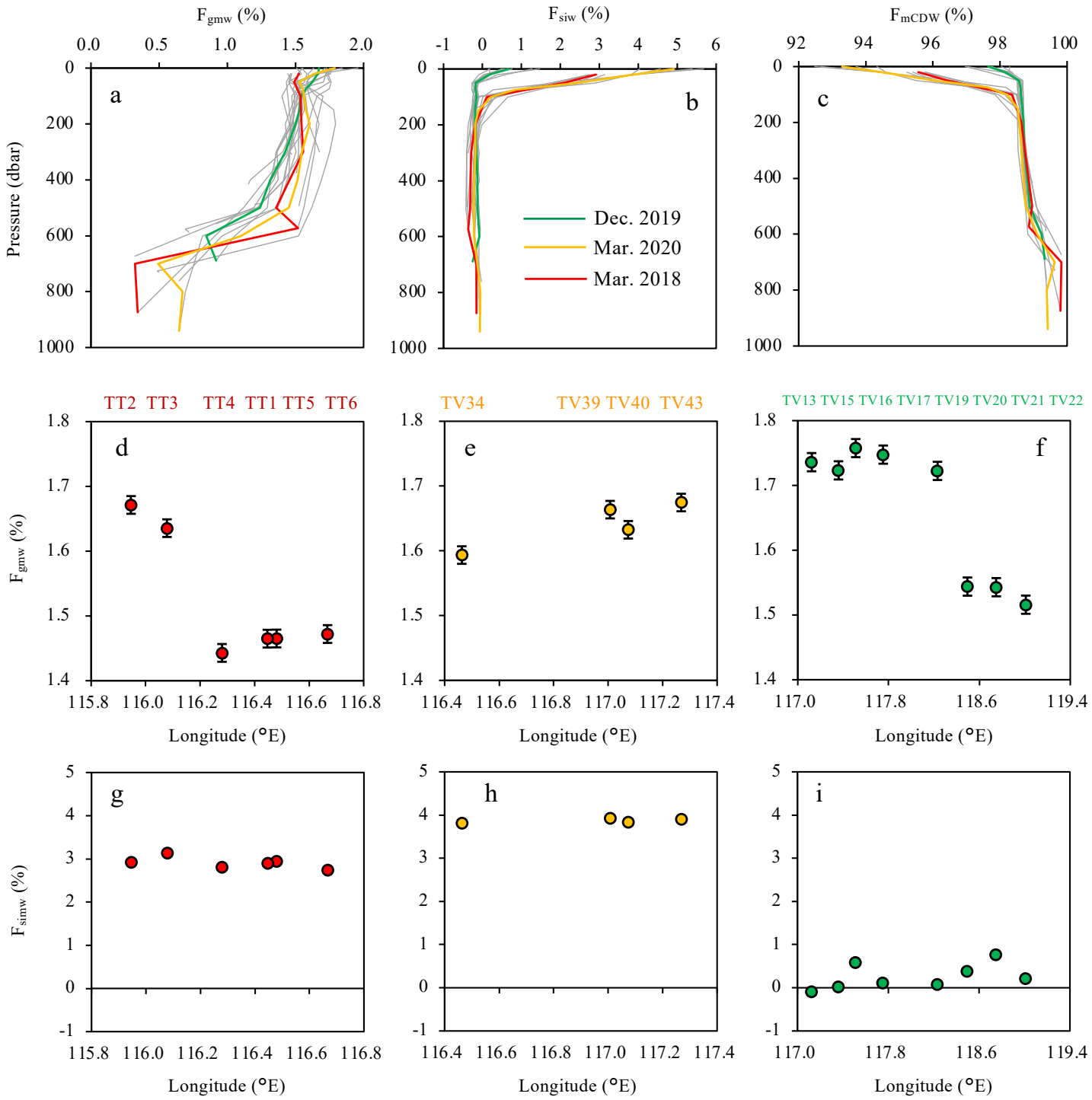

Figure 8_Tamura et al.

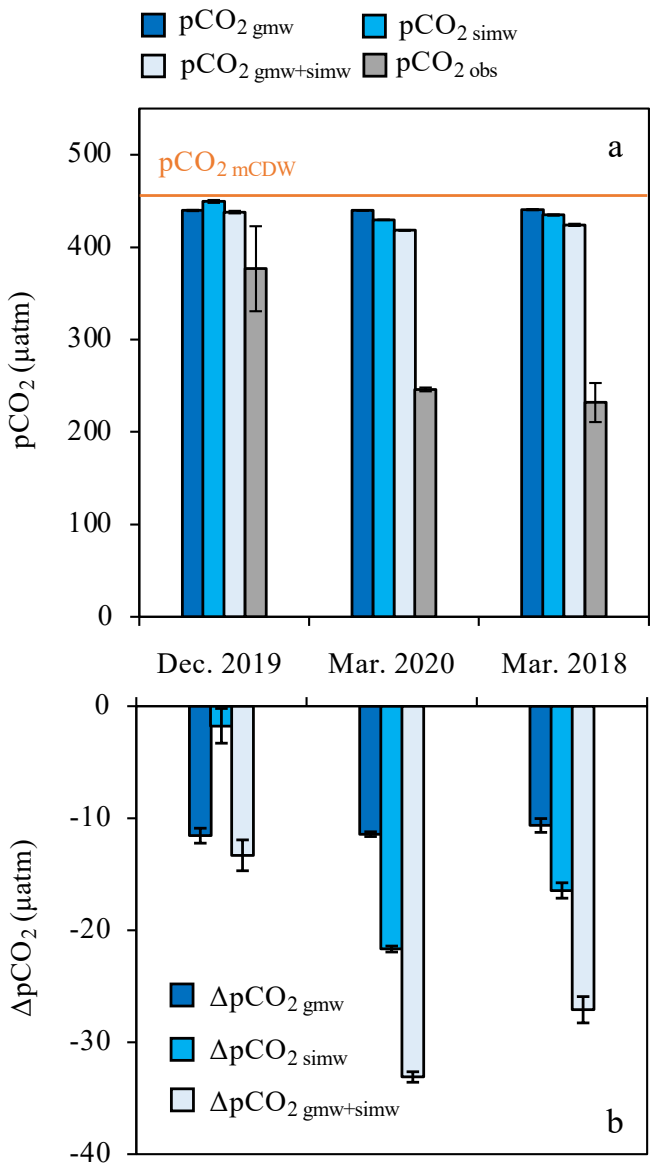

Figure 9_Tamura et al.

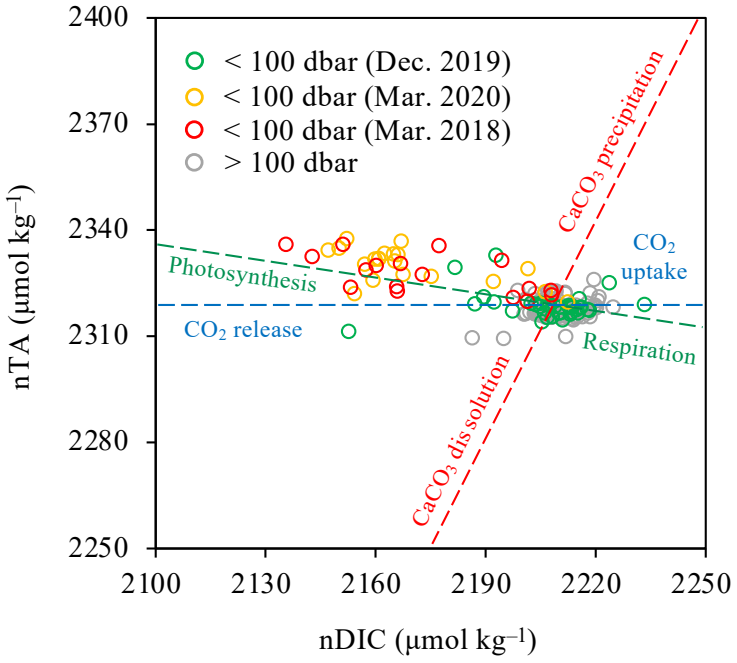

Figure 10_Tamura et al.

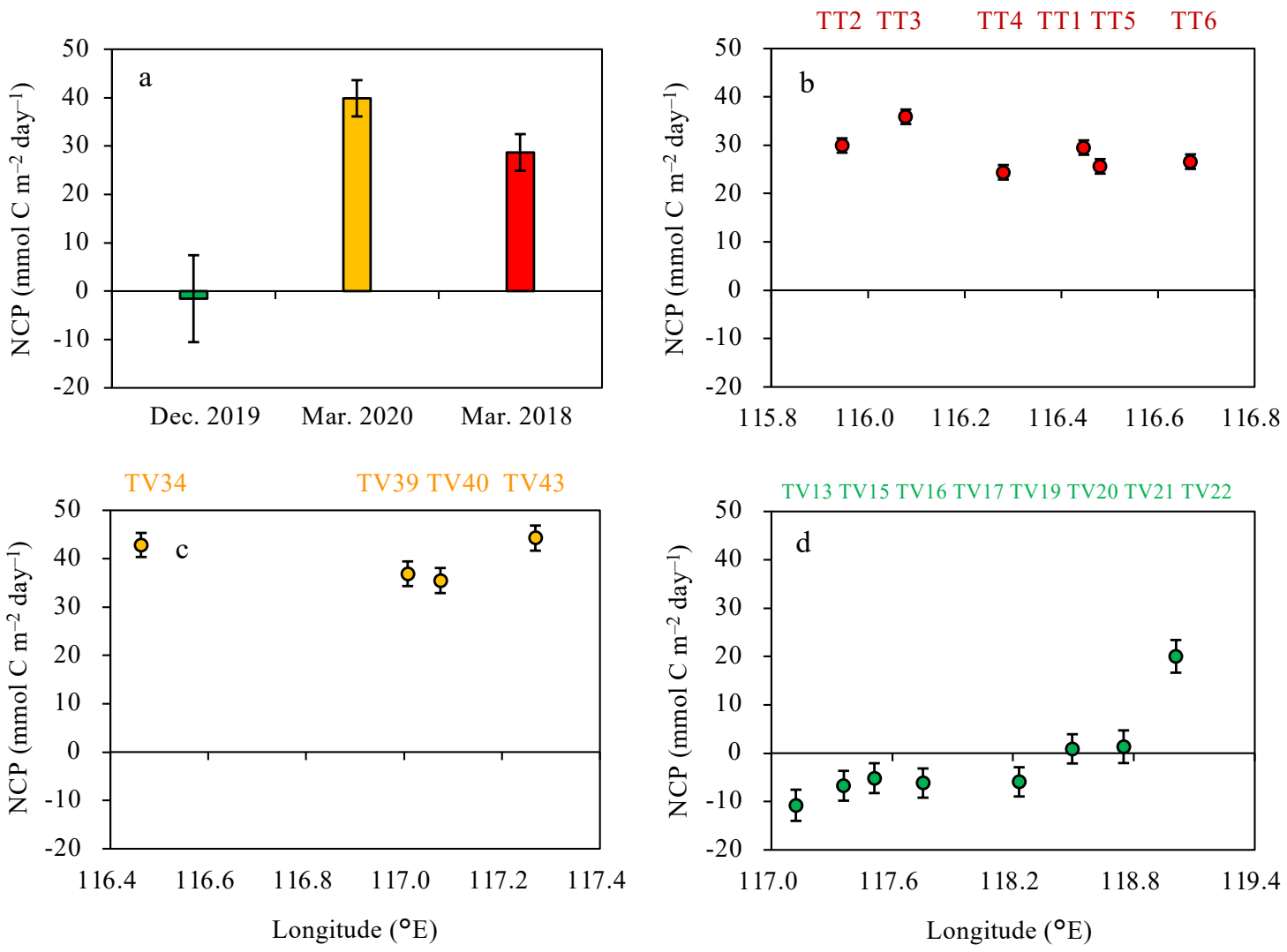

Figure 11_Tamura et al.

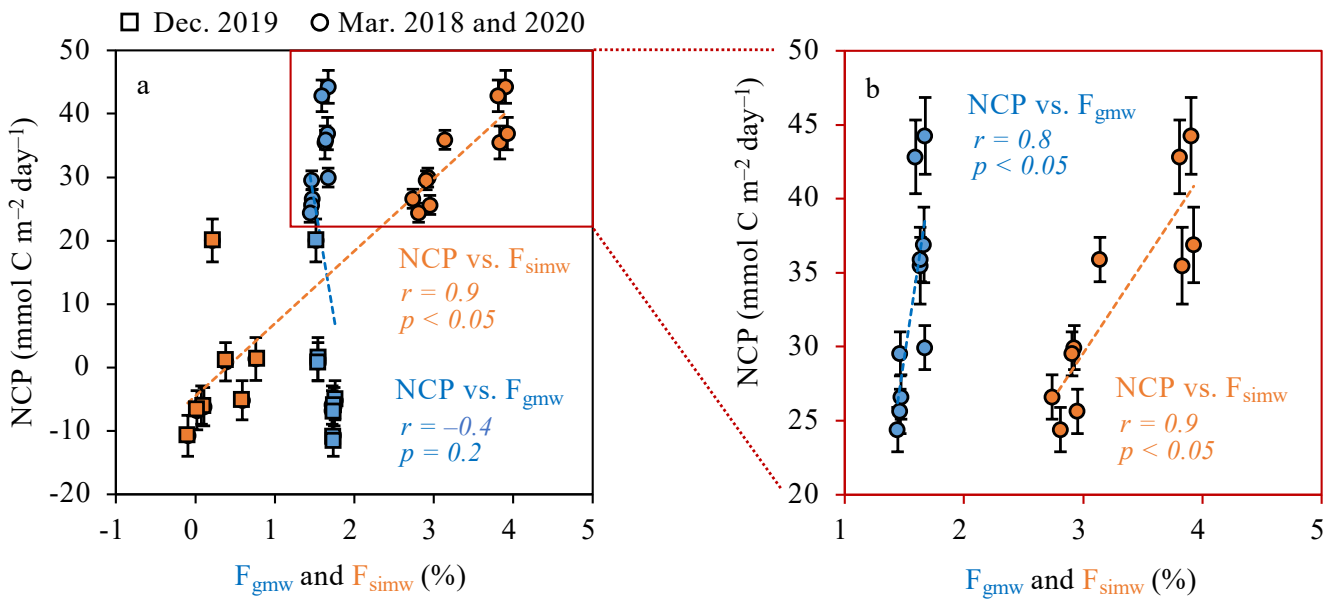

Figure 12_Tamura et al.

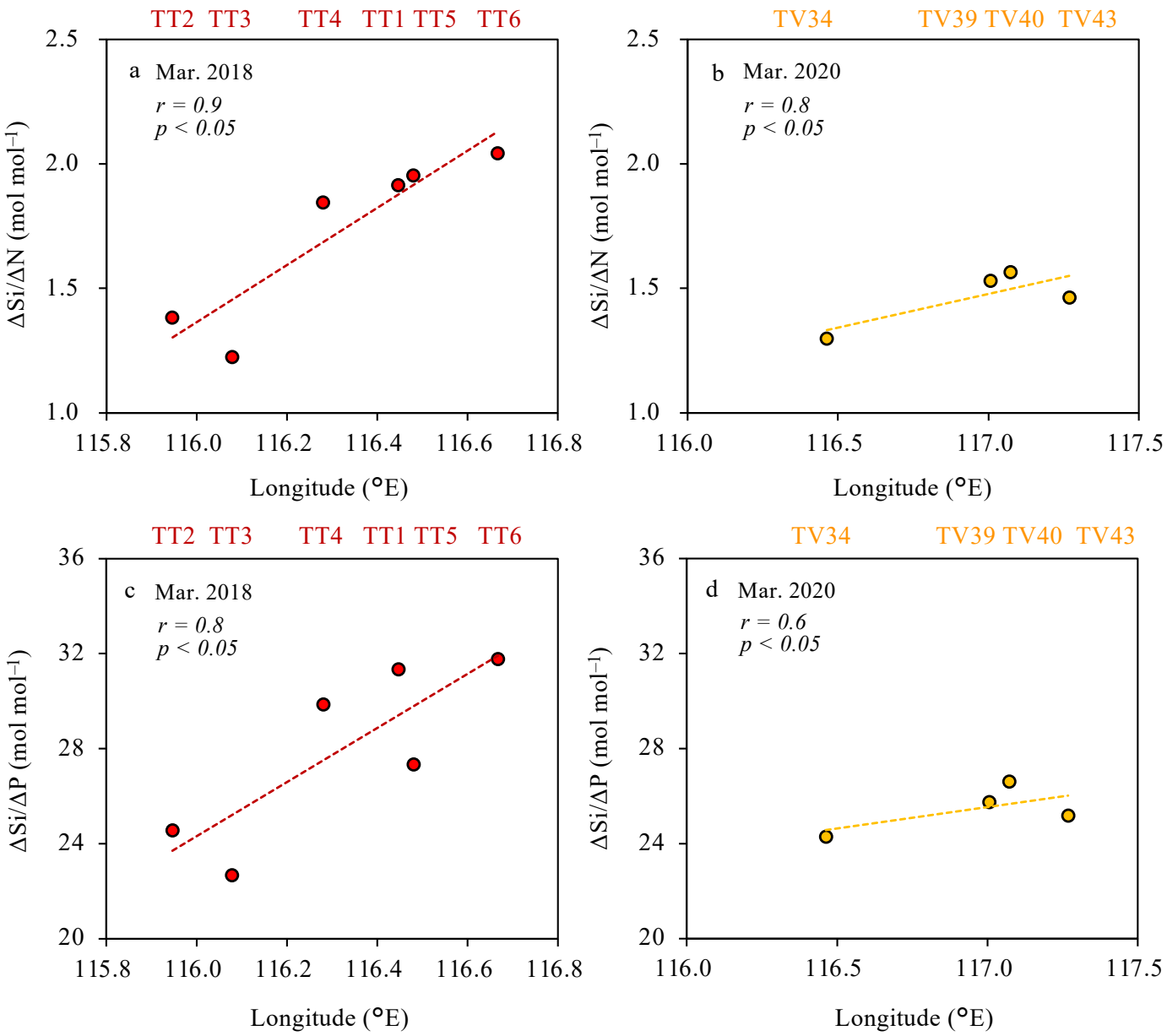

Figure 13_Tamura et al.

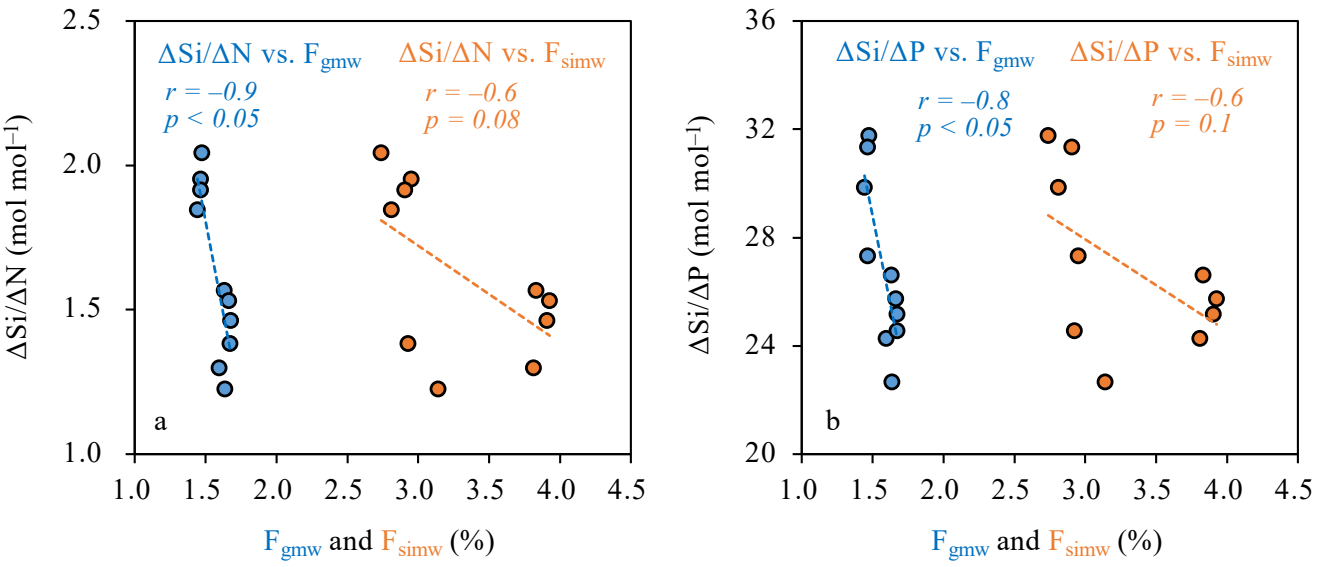

Figure 14_Tamura et al.

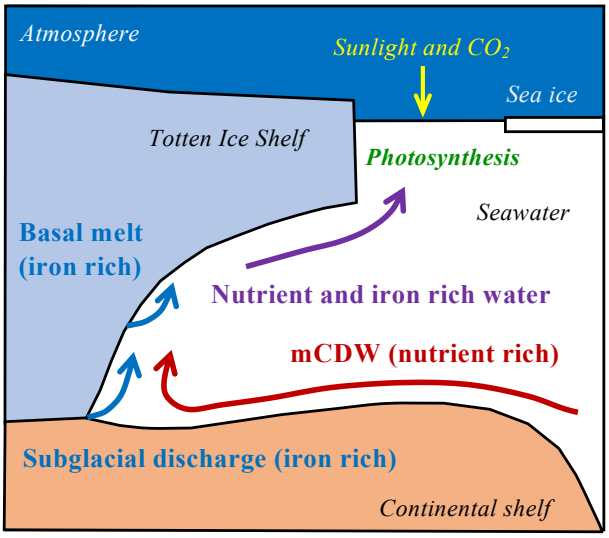

Figure 15_Tamura et al.

Table 1. Mean and standard deviation for DIC, TA, $\delta^{18}O$, NO_3^-, PO_4^{3-}, and $Si(OH)_4$ for each water mass and month.

Month	Water Mass	DIC	TA	$\delta^{18}O$	NO_3^-	PO_4^{3-}	$Si(OH)_4$
December	Surface	2194 ± 15	2305 ± 4	–0.55 ± 0.03	30.4 ± 1.3	2.05 ± 0.10	66.0 ± 6.8
	WW	2204 ± 3	2312 ±1	–0.51 ± 0.01	31.0 ± 0.3	2.08 ± 0.02	60.3 ± 3.1
	mCDW	2227 ± 8	2325 ± 8	–0.31 ± 0.04	32.2 ± 0.2	2.57 ± 0.55	79.7 ± 7.5
March	Surface	2086 ± 12	2253 ± 11	–0.49 ± 0.02	20.5 ± 1.9	1.38 ± 0.10	45.0 ± 0.7
	WW	2202 ± 4	2312 ± 2	–0.53 ± 0.04	32.2 ± 0.4	2.06 ± 0.08	63.9 ± 4.1
	mCDW	2233 ± 6	2337 ± 7	–0.21 ± 0.04	33.6 ± 0.7	2.21 ± 0.08	89.5 ± 8.0

Units were μmol kg^{-1} for DIC and TA, ‰ for $\delta^{18}O$, and μmol L^{-1} for nutrients.